Chapter 4
Quantum Dynamics Effects on Amplitude-Frequency Response of Superharmonic Resonance of Second-Order of Electrostatically Actuated NEMS Circular Plates

Dumitru I. Caruntu, Julio S. Beatriz

Abstract This work deals with the effects of Casimir and/or van der Waals forces (quantum dynamics phenomena) on the amplitude-frequency response of the superharmonic resonance of second-order of axisymmetric vibrations of electrostatically actuated nanoelectromechanical systems (NEMS) clamped circular plates. Electrostatic actuation consists of alternating current (*AC*) voltage of magnitude to produce hard excitations and of frequency near one fourth the natural frequency of the clamped circular plate. The intermolecular forces Casimir and van der Waals, damping force, and electrostatic force are the forces acting on the NEMS plate. Six Reduced Order Models (ROMs) with one and up to 6 modes of vibration are used. The ROM with one mode of vibration is solved using the Method of Multiple Scales (MMS) in which the hard excitations are modeled using first-order and second-order models of hard excitations electrostatic force. Also, Taylor polynomials up to 25th degree are used to approximate the electrostatic, Casimir and van der Waals forces in the ROM with one mode of vibration. MMS predicts the amplitude-frequency response (bifurcation diagram) of the resonance. The other ROMs, using from two to six modes of vibration are solved using two methods, namely continuation and bifurcation using AUTO software package to predict the amplitude-frequency response, and numerical integration using Matlab to predict time responses of the NEMS plate. The amplitude-frequency response predicts a softening effect, and the existence of three branches, two stable and one unstable. A saddle-node bifurcation point of amplitude of 0.24 of the gap, and end points of amplitudes of 0.66 and 0.75 of the gap of unstable and stable branches, respectively, are predicted. The increase of Casimir and/or van der Waals forces shifts the branches, bifurcation points, and endpoints to lower frequencies.

D. I. Caruntu, J. S. Beatriz
University of Texas Rio Grande Valley, Mechanical Engineering Department, Edinburg, Texas 78539, U.S.A.
e-mail: dumitru.caruntu@utrgv.edu, caruntud2@asme.org, dcaruntu@yahoo.com, julio.beatriz01@outlook.com

Keywords: MEMS, NEMS, non-linear, amplitude-frequency response, superharmonic resonance of second-order, circular plate resonators, Casimir effect, van der Waals effect

4.1 Introduction

Micro- and Nano-electromechanical systems (M/NEMS) are known for their small size, and variety of forms. By taking advantage of their size, these devices can be used in several applications, while maintaining high efficiency and performance (Ashoori et al, 2017). Their variety of shapes such as circular plates (Sajadi et al, 2018; Caruntu and Oyervides, 2017, 2016; Liao et al, 2009), beams (Caruntu et al, 2019, 2013; Zhang et al, 2015), membranes (Dorfmeister et al, 2018), carbon nanotubes (Caruntu and Juarez, 2019; Caruntu and Luo, 2014; Khadem et al, 2012), provide options that allow one to decide which benefits a specific application the most. These applications include, but are not limited to, micropumps (Wang and Fu, 2018; Nisar et al, 2008), ultrasonic transducers (Ahmad and Pratap, 2010), energy harvesters (Zhang et al, 2015), and shock switches (Khadem et al, 2012). Furthermore, these systems are able to perform with a huge assortment of actuation methods, such as thermal actuation (Varona et al, 2007), piezoelectric (Wang and Fu, 2018; Nisar et al, 2008; Maurini et al, 2006), and electrostatic (Caruntu and Juarez, 2019; Nisar et al, 2008). Electrostatic actuation in M/NEMS plates involves the use of parallel plates, one of which is fixed and the other flexible. By applying a voltage between the plates, an electrostatic force is induced between the plates, which leads to a deformation of the flexible plate. By applying an alternating current (*AC*) voltage, the flexible plate vibrates. However, these devices might also have a direct current (*DC*) voltage component, which induces a static deflection onto the flexible plate (Liao et al, 2009).

The frequency and amplitude of the *AC* voltage has a direct effect on the behavior of the system. As these systems are non-linear, changing the voltage can have an effect on the stability of the system. As shown by Sajadi et al (2018), different parameters such as differential pressure can lead to unexpected behavior, i.e increased stability with increasing voltage. Other parameters such as intermolecular forces Casimir and van der Waals should be taken into consideration when designing NEMS. Intermolecular forces are significant at nano scales, reaching the point of the intermolecular forces overcoming the natural resistance of the structure (Batra et al, 2008). It should be said that Casimir and van der Waals forces cannot occur at the same time. They describe the same phenomenon at different scales. For gaps greater than 100 nm, Casimir force describes the intermolecular interaction, and for gaps less than 50 nm, van der Waals force (Caruntu and Reyes, 2020; Caruntu et al, 2016; Batra et al, 2008). If one reaches a critical voltage, or a combination of factors in the system, pull-in can occur. Pull-in is a phenomenon in which the flexible plate gets in contact with the ground plate (Caruntu and Reyes, 2020; Liao et al, 2009). This occurs when the attracting forces overcome the natural resistance of the structure.

M/NEMS circular plates are also affected by damping (Ishfaque and Kim, 2017; Shabani et al, 2013) or surface effects (Lin et al, 2018). Damping depends on the environment in which the M/NEMS are being used. Shabani et al (2013) mentioned that if the fluid is a liquid, the model should take into consideration the damping effect, as well as added mass. This has a great effect on the behavior of the system, due to the energy loss. Designs such as perforated circular plates (Ishfaque and Kim, 2017) were also taken into consideration in order to control the level of damping the system is influenced by. Surface effects including surface stress and elasticity affect the pull-in voltage. Surface effects are significant if the circular plates are quite thin or have a large surface to volume ratio (Lin et al, 2018). A variety of models have been reported in the literature. Such models include the Kirchoff thin plate theory (Anjomshoa and Tahani, 2016; Rahim, 2010a), or the Mindlin plate theory (Rahim, 2010a). The Mindlin plate theory takes into consideration the shear strain, while the Kirchhoff does not.

Secondary resonances that occur at fractions of the natural frequency and under hard excitations, i.e. superharmonic resonance, constitute a very important topic. Many studies have been conducted on M/NEMS under secondary resonances (Caruntu et al, 2021, 2019; Kacem et al, 2012; Najar et al, 2010; Nayfeh and Younis, 2005). Better understanding of the behavior of the system, would help to better design and optimize it. Superharmonic resonances occur at a frequency less than that of the natural frequency, causing larger than normal amplitudes to occur due to hard excitations. As shown by Kacem et al (2012); Najar et al (2010); Nayfeh and Younis (2005), the behavior of a system varies, and depending on the situation, softening and hardening behavior can occur. Furthermore, Najar et al (2010) showed that even superharmonic resonances behave differently.

This paper investigates the amplitude-frequency response of superharmonic resonance of second-order of electrostatically actuated M/NEMS clamped circular plate resonators. Only AC voltage is considered in this work. This investigation has been conducted using Reduced Order Models (ROMS) with a number of modes of vibration (Caruntu et al, 2013) from one to six. These models have been solved using the Method of Multiple Scales (MMS), continuation and bifurcation using AUTO, and numerical integration using Matlab (*fsolve* and *ode15s*). The effects of various parameters, such as voltage, damping, Casimir and van der Waals effects are reported. The effect of higher degree Taylor polynomials approximating electrostatic, Casimir, and van der Waals forces in the ROM with one mode of vibration on the amplitude-frequency response is also reported. The effects of parameters voltage and damping on the amplitude-frequency response are reported as well. ROMs are also numerically integrated to predict time responses. While similar methods have been used for circular plates (Caruntu and Oyervides, 2017, 2016), this is the first time a second-order model for hard excitations is used, and an investigation regarding the effect of the degree of Taylor polynomials approximating the electrostatic, Casimir and van der Waals forces on the amplitude-frequency response are conducted. In comparison to data reported in the literature, the behavior of the clamped circular plate is similar to Kim and Lee (2015); Najar et al (2010) who investigated other structures than circular plates. For example, (Kim and Lee, 2015) used a model in-

cluding only *AC* which causes the super harmonic resonance of order two to appear in carbon nanotubes. They reported a more linear behavior. This is different from the predictions of present work for clamped circular plates in which the branches split at higher amplitudes showing a strong nonlinear behavior. Similar behavior with (Kim and Lee, 2015) is shown for clamped circular plates. Najar et al (2010) focused on cantilevers. In their case the branches split as in present work. However their results show a hardening effect, not a softening effect as in present work.

The novelty of this paper consists of:

1. Reporting the amplitude-frequency response of superharmonic resonance of M/NEMS clamped circular plates,
2. in order to include quantum dynamics effects such as Casimir and van der Waals forces.
3. The amplitude-frequency response (bifurcation diagram) predicts the existence of a saddle-node bifurcation at an amplitude around 0.25 of the gap and three branches, two stable and one unstable.
4. The two branches in higher amplitudes are shown to have endpoints around 0.7 of the gap, which leads to a narrow interval for which pull-in occurs.
5. Six ROMs are used in this investigation using from one to six modes of vibration (terms).
6. The ROM using one term (1T ROM) is solved using MMS,
7. in which two models of hard excitations are proposed,
8. and an investigation regarding the degree of Taylor polynomials approximating the electrostatic, Casimir and van der Waals forces is conducted.
9. The other ROMs using from two to six terms are solved using a continuation and bifurcation software package AUTO, and are numerically integrated using Matlab.
10. It is shown that ROM with 6 modes of vibration (6T ROM) is the one with the best prediction for all amplitudes in the bifurcation diagram.
11. This work predicts that both Casimir and van der Waals forces in NEMS shift the steady-state amplitudes in the bifurcation diagram to lower frequencies and increase the softening effect.
12. It also predicts that hard excitations with dimensionless voltage parameter $\delta > 3$ and dimensionless damping parameter $b \leq 0.025$ lead to superharmonic resonance of second-order. Several papers used MMS or the ROM with more than one mode of vibration to simulate the behavior of these systems, whether they were cantilevers (Caruntu et al, 2021, 2019, 2013; Liu et al, 2014; Kahrobaiyan et al, 2011; Najar et al, 2010), carbon nanotubes (Caruntu and Juarez, 2019; Caruntu and Luo, 2014; Kim and Lee, 2015), or plates (Caruntu and Oyervides, 2017, 2016; Sharafkhani et al, 2012; Batra et al, 2008). Most of the literature, except for (Kim and Lee, 2015; Liu et al, 2014), model electrostatic actuation with both *DC* and *AC*. Yet, these exceptions do not consider an MMS model for hard excitation for circular plates.

4.2 Differential Equation of Motion

Figure 4.1 shows an M/NEMS circular plate, which is parallel to a ground plate at a gap distance d. The radius and thickness of the plate are R and h, respectively. Between the M/NEMS circular plate and the ground plate there is an *AC* voltage of amplitude V_0 of frequency $\hat{\Omega}$. The *AC* voltage produces an electrostatic force between the circular plate and the ground plate, which leads to the circular plate into vibrations with the dimensional deflections $\hat{u}(\hat{r},\hat{t})$, where $\hat{r}$, $\hat{t}$ are the dimensional current radius and dimensional time, respectively. This work considers only axisymmetrical vibrations. The partial differential equation of motion describing the clamped circular plate (Caruntu and Oyervides, 2017, 2016), Fig. 4.1, is based on Kirchoff plate theory (classical plate theory) valid for thin plates (Rahim, 2010b; Lee et al, 1998; Baecker et al, 2015), i.e. thickness to diameter radius ratio less than 0.05 (Zietlow et al, 2012), and it includes Casimir and van der Waals forces:

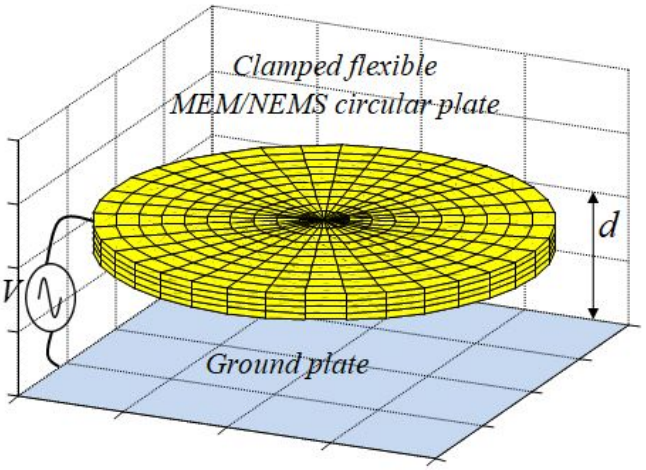

Fig. 4.1 Circular plate suspended above ground plate

$$\rho h\frac{\partial^2\hat{u}(\hat{t},\hat{r})}{\partial\hat{t}^2}+2c_1\frac{\partial\hat{u}(\hat{t},\hat{r})}{\partial\hat{t}}+D\left[\frac{\partial^4\hat{u}(\hat{t},\hat{r})}{\partial\hat{r}^4}+\frac{2}{\hat{r}}\frac{\partial^3\hat{u}(\hat{t},\hat{r})}{\partial\hat{r}^3}-\frac{1}{\hat{r}^2}\frac{\partial^2\hat{u}(\hat{t},\hat{r})}{\partial\hat{r}^2}\right.$$
$$\left.+\frac{1}{\hat{r}^3}\frac{\partial\hat{u}(\hat{t},\hat{r})}{\partial\hat{r}}\right]=\frac{\epsilon^*V_0^2\cos^2\hat{\Omega}\hat{t}}{2[d-\hat{u}(\hat{t},\hat{r})]^2}+\frac{H}{6\pi[d-\hat{u}(\hat{t},\hat{r})]^3}+\frac{\bar{h}c\pi^2}{240[d-\hat{u}(\hat{t},\hat{r})]^4}\,, \tag{4.1}$$

where ρ is plate density, c_1 damping coefficient, D flexural rigidity, ϵ^* electrical permitivity, V_0 magnitude of *AC* voltage, H Hamaker constant, $\bar{h}$ reduced Plank constant, and c the speed of light in vacuum. The following dimensionless variable are introduced: dimensionless radial coordinate r, dimensionless deflection u and

dimensionless time t. They are written in terms of the dimensional variables $\hat{r}$, $\hat{u}$ and $\hat{t}$ (Caruntu and Oyervides, 2017, 2016) are as follows:

$$r = \frac{\hat{r}}{R}\ ,\ \ u = \frac{\hat{u}}{d}\ ,\ \ t = \hat{t}\sqrt{\frac{D}{\rho h R^4}}\ . \tag{4.2}$$

The dimensionless partial-differential equation of motion to include both intermolecular forces, Casimir and van der Waals, is given by

$$\frac{\partial^2 u(t,r)}{\partial t^2} + b\frac{\partial u(t,r)}{\partial t} + P[u] = \frac{\delta\cos^2\Omega t}{[1-u(t,r)]^2} + \frac{\mu}{[1-u(t,r)]^3} + \frac{\alpha}{[1-u(t,r)]^4}\ , \tag{4.3}$$

where μ and α cannot be different than zero at the same time since Casimir and van der Waals forces describe the same phenomenon but at different scales. Operator $P[u]$ is given by

$$P[u] = \frac{\partial^4 u(t,r)}{\partial r^4} + \frac{2}{r}\frac{\partial^3 u(t,r)}{\partial r^3} - \frac{1}{r^2}\frac{\partial^2 u(t,r)}{\partial r^2} + \frac{1}{r^3}\frac{\partial u(t,r)}{\partial r}\ . \tag{4.4}$$

The dimensionless parameters are as follows: Ω is the dimensionless *AC* frequency, b is dimensionless damping parameter, α is the dimensionless Casimir parameter, μ is the dimensionless van der Waals parameter, δ the dimensionless voltage parameter and ω_i are the dimensionless natural frequencies of clamped circular plates. These dimensionless parameters are as follows:

$$\begin{gathered}\Omega = \hat{\Omega}\sqrt{\frac{\rho h R^4}{D}}\ ,\ \ b = 2c_1\sqrt{\frac{R^4}{\rho h D}}\ ,\ \ \delta = \frac{R^4\epsilon^* V_0^2}{2Dd^3}\ ,\ \ \alpha = \frac{R^4\bar{h}c\pi^2}{240Dd^5}\ ,\\ \mu = \frac{R^4 H}{6\pi D d^4}\ ,\ \ \omega_i = \hat{\omega}_i\sqrt{\frac{\rho^h R^4}{D}}\ ,\ \ D = \frac{Eh^3}{12(1-\nu^2)}\ ,\end{gathered} \tag{4.5}$$

where E is the Young's modulus, ν is Poisson's ratio. Furthermore, $\hat{\omega}_i$ are the dimensional natural frequencies. The first six dimensionless natural frequencies of clamped circular plate are given in Table 4.1. The values of the constants of the

Table 4.1 First six natural frequencies

	$i=1$	$i=2$	$i=3$	$i=4$	$i=5$	$i=6$
ω_i	10.2158	39.7711	89.1041	158.1842	247.0064	355.5693

system are given below in Table 4.2, and the dimensional system parameters are given in Tables 4.3, 4.4, and 4.5 for 3 cases, namely electrostatic, $\alpha = \mu = 0$, in Eq. (4.3), Casimir, $\mu = 0$; and van der Waals, $\alpha = 0$, respectively. The material properties are of polysilicon (Ouakad, 2017; Lee et al, 1998; Sharpe et al, 1997) and are in Table 4.2. The plate dimensions in Tables 4.3-4.5 satisfy criteria for thin

plates from the classical plate theory (Zietlow et al, 2012). Tables 4.2-4.5 result in the dimensionless system parameters shown in Table 4.6. The dimensionless mode

Table 4.2 Constants

Young's modulus	E	169 GPa
Poisson's ratio	ν	0.22
Permitivity of free space	ϵ^*	8.854×10^{-12} C^2/N/m^2
Density of material	ρ	2330.0 kg/m^3
Planck's constant / 2π	$\bar{h}$	1.0546×10^{-34} m^2 kg/s
Speed of light in vacuum	C	299 972 km/s
Hamaker constant	H	4.4×10^{-19} J

Table 4.3 Dimensional parameters, electrostatic case MEMS

Initial gap distance	d	1.014 μm
Plate thickness	h	3.01 μm
Radius of plate	R	250 μm
Damping	c_1	10.64 N s/m^3
Voltage	V_0	9.865 V

Table 4.4 Dimensional parameters, Casimir case NEMS

Initial gap distance	d	0.15 μm
Plate thickness	h	0.4 μm
Radius of plate	R	57.675 μm
Damping	c_1	3.5307 N s/m^3
Voltage	V_0	0.5109 V

Table 4.5 Dimensional parameters, van der Waals case NEMS

Initial gap distance	d	0.05 μm
Plate Thickness	h	0.0301 μm
Radius of Plate	R	2.1561 μm
Damping	c_1	14.305 N s/m^3
Voltage	V_0	1.4522 V

Table 4.6 Dimensionless system parameters

Voltage Parameter	δ	4.0
Damping Parameter	b^*	0.025
Casimir Parameter	α	0.2
van der Waals parameter	μ	0.2

shapes ϕ_i of the clamped circular plates are given in terms of J_0 and I_0 which are Bessel functions of first kind and modified first kind, respectively, as follows:

$$\phi_i(r) = \frac{J_0\left(\sqrt{\omega_i} \cdot r\right)}{J_0\left(\sqrt{\omega_i}\right)} - \frac{I_0\left(\sqrt{\omega_i} \cdot r\right)}{I_0\left(\sqrt{\omega_i}\right)} \tag{4.6}$$

The dimensionless mode shapes form an orthonormal set. The relationship between the mode shapes ϕ_1 and the natural frequency (Rao, 2007) is given by

$$\phi_i^{(4)} + \frac{2}{r}\phi_i''' - \frac{1}{r^2}\phi_i'' + \frac{1}{r^3}\phi_i' = \omega_i^2\phi_i \tag{4.7}$$

4.3 Superharmonic Resonance of Second-Order

The dimensionless frequency Ω of the *AC* voltage, that produces electrostatic force, is considered to be nearly one fourth of the natural frequency

$$\Omega = \frac{\omega_1}{4} + \epsilon\sigma \tag{4.8}$$

where σ is the detuning parameter, and ϵ a bookkeeping parameter used in MMS. The bookkeeping parameter ϵ is assumed to be small such that it indicates a small detuning parameter in Eq. (4.8), and indicates the small terms in the equations of motion of Sections 4.4 and 4.6. The dimensionless voltage V, Eq. (4.3), is given by

$$V = \sqrt{\delta}\cos\Omega t \tag{4.9}$$

As the electrostatic force is proportional to the square of the voltage, the frequency of the electrostatic force is twice the *AC* frequency. This leads to superharmonic resonance of the second-order. The square of the dimensionless voltage is as follows:

$$V^2 = \delta\cos^2\Omega t = \delta\frac{1+cos2\Omega t}{2} = \delta\Big(\frac{1}{2} + \frac{e^{2i\Omega t}+e^{-2i\Omega t}}{4}\Big) \tag{4.10}$$

4.4 Method of Multiple Scales: First-Order Hard Excitations Model

All forces at the right-hand side of Eq. (4.3), are approximated by Taylor polynomials. In the first-order hard excitations model, the first term of the Taylor polynomial of the electrostatic force on the right-hand side of the equation is being treated as significant so it does not have the bookkeeping parameter ϵ as coefficient. All other terms of the Taylor polynomial of the electrostatic force, the Taylor polynomials of Casimir and/or van der Waals forces, as well as the damping force, are considered small, so all these terms have the bookkeeping parameter ϵ as coefficient as follows:

$$\begin{aligned}\frac{\partial^2 u}{\partial t^2} + \epsilon b\frac{\partial u}{\partial t} + P[u] &= \delta\frac{1+\cos 2\Omega t}{2} + \epsilon\delta(2u+3u^2+4u^3)\frac{1+\cos 2\Omega t}{2}\\ &+ \epsilon\mu(1+3u+6u^2+10u^3) + \epsilon\alpha(1+4u+10u^2+20u^3)\,,\end{aligned} \tag{4.11}$$

where $P[u]$ is given by Eq. (4.4). The first-order hard excitations model is also called one term no epsilon (1TnE) model in this work. The solution of Eq. (4.11) uses the first mode of vibration that is given by

$$u(t.r) = u_1(t)\phi_1(r) \ , \tag{4.12}$$

where $u_1(t)$ is a function of time to be determined and $\phi_1(r)$ is the first modeshape of the clamped circular plate. Assume a uniform expansion (Caruntu et al, 2021) of $u_1(t)$ as follows:

$$u_1(t) = u_{10}(t) + \epsilon u_{11}(t) \ . \tag{4.13}$$

Two time scales are considered, a fast time scale $T_0 = t$ and a slow time scale $T_1 = \varepsilon \cdot t$. The partial derivatives with respect to the time scales are given by

$$D_0 = \frac{\partial}{\partial T_0}, \quad D_1 = \frac{\partial}{\partial T_1} \tag{4.14}$$

and the time derivatives become

$$\frac{\partial}{\partial t} = D_0 + \epsilon D_1, \quad \frac{\partial^2}{\partial t^2} = D_0^2 + 2\epsilon D_1 D_0 \ . \tag{4.15}$$

Substituting Eqs. (4.12)-(4.15) into Eq. (4.11), using Galerkin method by multiplying the resulting equation by $r\phi_1$ and integrating from 0 to 1, introducing the following notations

$$g_1 = \int_0^1 r\phi_1 dr, g_2 = \int_0^1 r\phi_1^2 dr, g_3 = \int_0^1 r\phi_1^3 dr, g_4 = \int_0^1 r\phi_1^4 dr \tag{4.16}$$

and then collecting the terms having the same power of ϵ, a zero-order problem and a first-order problem result as follows:

$$\epsilon^0 : D_0^2 u_{10} + u_{10}\omega_1^2 = g_1\delta\left(\frac{1}{2} + \frac{e^{2i\Omega T_0} + e^{-2i\Omega T_0}}{4}\right) \tag{4.17}$$

$$\begin{aligned}\epsilon^1 : {} & D_0^2 u_{11} + u_{11}\omega_1^2 = -2D_0 D_1 u_{10} - bD_0 u_{10} + \delta(2u_{10} + 3u_{10}^2 g_3 \\ & + 4u_{10}^3 g_4)\left(\frac{1}{2} + \frac{e^{2i\Omega T_0} + e^{-2i\Omega T_0}}{4}\right) + \mu(g_1 + 3u_{10} + 6u_{10}^2 g_3 + 10u_{10}^3 g_4) \\ & + \alpha(g_1 + 4u_{10} + 10u_{10}^2 g_3 + 20u_{10}^3 g_4)\end{aligned} \tag{4.18}$$

It should be noted that g_2 = 1. The zero-order problem Eq. (4.17) has the following solution

$$u_{10} = Ae^{i\omega_1 T_0} + \bar{A}e^{-i\omega_1 T_0} + \Lambda e^{2i\Omega T_0} + \Lambda e^{-2i\Omega T_0} + K \ , \tag{4.19}$$

where Λ and K are given by

$$\Lambda = \frac{\delta}{4}\frac{g_1}{(\omega_1^2 - 4\Omega^2)} \ , \quad K = \frac{\delta g_1}{2\omega_1^2} \ . \tag{4.20}$$

After substituting Eq. (4.19) into Eq. (4.18), the secular terms are collected and their sum is set to zero. The complex amplitude A and its conjugate $\bar{A}$, written in terms

of the real phase β_1 and real amplitude a_1 are as follows:

$$A=\frac{1}{2}a_1e^{i\beta_1}\ ,\ \ \bar{A}=\frac{1}{2}a_1e^{-i\beta_1}\ . \tag{4.21}$$

Substituting Eq. (4.21) into the secular terms equation, dividing the resulting equation by $e^{i\beta_1}$, and separating the real and imaginary parts, the following amplitude-phase differential equations result

$$\begin{aligned}a_1'=&-\frac{b}{2}a_1+\frac{\Lambda sin\gamma}{2\omega_1}\Big\{\delta+g_3\big[3\delta(\Lambda+K)+4\Lambda(3\mu+5\alpha)\big]\\&+g_4\big[\delta(12K\Lambda+8\Lambda^2+6K^2+\frac{3}{2}a_1^2)+60K\Lambda(\mu+2\alpha)\big]\Big\}\ ,\end{aligned} \tag{4.22}$$

$$\begin{aligned}\gamma'=&\,4\sigma+\frac{1}{2\omega_1}\big[\delta+3\mu+4\alpha\big]+\frac{\delta}{2a_1\omega_1}\Lambda cos\gamma\\&+\frac{1}{a_1\omega_1}\Big\{g_3\big[\frac{3}{2}\delta(K+\Lambda)(a_1+\Lambda cos\gamma)+2(3\mu+5\alpha)(\Lambda^2cos\gamma+a_1K)\big]\\&+g_4\big[3\delta(K^2a_1+2K\Lambda a_1+2\Lambda^2a_1+\frac{1}{4}a_1^3+\Lambda(2K\Lambda+\frac{4}{3}\Lambda^2+K^2\\&+\frac{3}{4}a_1^2)cos\gamma)+15(\mu+2\alpha)(2K\Lambda^2cos\gamma+a_1K^2+2a_1\Lambda^2+\frac{1}{4}a_1^3)\big]\Big\}\ ,\end{aligned} \tag{4.23}$$

where $'$ is the derivative with respect to the slow scale T_1, and γ is given by

$$\gamma=4\sigma T_1-\beta_1\ . \tag{4.24}$$

In order to find the steady-state amplitudes, the derivatives of the amplitude a_1 and phase γ are set to zero ($a_1'=\gamma'=0$). The resulting equations predicting the amplitude-frequency response are

$$\sigma=\frac{-1}{4a_1\omega_1}(A_1a_1^3+B_1a_1^2+C_1a_1+D_1)\ , \tag{4.25}$$

where

$$\begin{aligned}A_1=&\,\frac{3}{4}g_4(\delta+5\mu+10\alpha)\\B_1=&\,\frac{9}{4}\delta g_4\Lambda cos\gamma\\C_1=&\,\frac{\delta}{2}+\frac{3}{2}\mu+2\alpha+g_3\big[\frac{3}{2}\delta(\Lambda+K)+2K(3\mu+5\alpha)\big]\\&+g_4\big[3\delta(K^2+2\Lambda^2+2K\Lambda)+15(\mu+2\alpha)(K^2+2\Lambda^2)\big]\\D_1=&\,\Lambda cos\gamma\Big\{\frac{1}{2}\delta+g_3\big[\frac{3}{2}\delta(\Lambda+K)+2\Lambda(3\mu+5\alpha)\big]\\&+g_4\big[\delta(3K^2+4\Lambda^2+6K\Lambda)+30K\Lambda(\mu+2\alpha)\big]\Big\}\end{aligned} \tag{4.26}$$

and

$$a_1 = \frac{-B_2 \pm \sqrt{B_2^2 - 4A_2C_2}}{2A_2} \,, \tag{4.27}$$

where

$$\begin{aligned} A_2 &= \frac{3\delta g_4 \Lambda}{4\omega_1} sin\gamma \\ B_2 &= \frac{-b}{2} \\ C_2 &= \frac{\Lambda sin\gamma}{\omega_1}\Big\{\frac{1}{2}\delta + g_3\big[\frac{3}{2}\delta(\Lambda + K) + 2\Lambda(3\mu + 5\alpha)\big] \\ &+ g_4\big[\delta(3K^2 + 4\Lambda^2 + 6K\Lambda) + 30\Lambda K(\mu + 2\alpha)\big]\Big\} \,. \end{aligned} \tag{4.28}$$

4.5 Stability Testing

In order to test the stability of the steady-state solutions of the system of equations (4.22 , 4.23) of the 1TnE electrostatic MMS model, the Jacobian

$$J = \begin{bmatrix} \frac{\partial a_1'}{\partial a_1} & \frac{\partial a_1'}{\partial \gamma} \\ \frac{\partial \gamma'}{\partial a_1} & \frac{\partial \gamma'}{\partial \gamma} \end{bmatrix} = \begin{bmatrix} V_1 & V_2 \\ V_3 & V_4 \end{bmatrix} \tag{4.29}$$

is needed. The eigenvalues of the Jacobian are given by

$$\det \begin{bmatrix} V_1 - \lambda & V_2 \\ V_3 & V_4 - \lambda \end{bmatrix} = 0 \,, \tag{4.30}$$

where

$$\begin{aligned} V_1 =& \frac{1}{2\omega_1}\Big(- b\omega_1 + 3\delta g_4 a_1 \Lambda \sin\gamma \Big) \,, \\ V_2 =& \frac{\Lambda\cos\gamma}{2g_2\omega_1}\big[\delta g_2 + 3\delta g_3(\Lambda + K) + \delta g_4(12K\Lambda + 8\Lambda^2 + 6K^2 + \frac{9}{2}a_1^2)\big] \,, \\ V_3 =& \frac{-\cos\gamma}{2a_1^2\omega_1}\big[\delta\Lambda + 3\delta g_3\Lambda(\Lambda + K) + g_4(12K\Lambda^2 - \frac{3a_1^3}{\cos\gamma} + 8\Lambda^3 + 6K^2\Lambda \\ & - \frac{9}{2}a_1^2\Lambda)\big] \,, \\ V_4 =& \frac{-\Lambda sin\gamma}{2a_1^2\omega_1}\big[\delta + 3\delta g_3(\Lambda + K) + \delta g_4(12K\Lambda + 8\Lambda^2 + 6K^2 + \frac{3}{2}a_1^2)\big] \,. \end{aligned} \tag{4.31}$$

4.6 Method of Multiple Scales: Second-Order Hard Excitations Model

In the second-order hard excitations model, the first two terms of the Taylor polynomial of the electrostatic force are considered significant, so they do not have the bookkeeping parameter ϵ as coefficient

$$\begin{aligned}&\frac{\partial^2 u}{\partial t^2}+\epsilon b\frac{\partial u}{\partial t}+P[u]=\delta\frac{1+\cos 2\Omega t}{2}\\&+2\delta u\frac{1+\epsilon\cos 2\Omega t}{2}+\epsilon\delta(3u^2+4u^3)\frac{1+\cos 2\Omega t}{2}\\&+\epsilon\mu(1+3u+6u^2+10u^3)+\epsilon\alpha(1+4u+10u^2+20u^3)\end{aligned}\tag{4.32}$$

The second-order hard excitations model is also called two-term no epsilon (2TnE) model in this work, This model allows for a better approximation of the solution. Using Eqs. (4.12-4.16) and Eq. (4.7), the resulting zero-order and the first-order problems are as follows:

$$\epsilon^0: D_0^2u_{10}+u_{10}\bar{\omega}_1^2=g_1\delta\left(\frac{1}{2}+\frac{e^{2i\Omega T_0}+e^{-2i\Omega T_0}}{4}\right),\tag{4.33}$$

$$\begin{aligned}&\epsilon^1: D_0^2u_{11}+u_{11}\bar{\omega}_1^2=-2D_0D_1u_{10}-bD_0u_{10}+\delta u_{10}\frac{e^{2i\Omega T_0}+e^{-2i\Omega T_0}}{2}\\&+\delta(3u_{10}^2g_3+4u_{10}^3g_4)\left(\frac{1}{2}+\frac{e^{2i\Omega T_0}+e^{-2i\Omega T_0}}{4}\right)\\&+\mu(g_1+3u_{10}+6u_{10}^2g_3+10u_{10}^3g_4)+\alpha(g_1+4u_{10}+10u_{10}^2g_3+20u_{10}^3g_4),\end{aligned}\tag{4.34}$$

where $\bar{\omega}_1^2$ is given by

$$\bar{\omega}_1^2=\omega_1^2-\delta\,.\tag{4.35}$$

The solution of the zero-order problem is as follows:

$$u_{10}=Ae^{i\bar{\omega}_1T_0}+\bar{A}e^{-i\bar{\omega}_1T_0}+\Lambda e^{2i\Omega T_0}+\Lambda e^{-2i\Omega T_0}+K\,,\tag{4.36}$$

where Λ and K are defined as

$$\Lambda=\frac{\delta}{4}\frac{g_1}{(\bar{\omega}_1^2-4\Omega^2)}\,,\quad K=\frac{\delta g_1}{2\bar{\omega}_1^2}\,.\tag{4.37}$$

Equation (4.36) is then substituted into the first-order problem Eq. (4.34), and the resulting equation is then expanded. This allows the secular terms for this resonance case to be gathered and their sum set equal to zero. The complex amplitudes Eq. (4.21), are substituted into the resulting equation, which is then divided by $e^{i\beta_1}$. Eq. (4.24) is used in the resulting equation and its real and imaginary parts are separated resulting into the following amplitude-phase differential equations

$$
\begin{aligned}
a_1' = &-\frac{b}{2}a_1 + \frac{\Lambda \sin\gamma}{2\bar{\omega}_1}\Big\{\delta + g_3\big[3\delta(\Lambda + K) + 4\Lambda(3\mu + 5\alpha)\big] \\
&+ g_4\big[\delta(12K\Lambda + 8\Lambda^2 + 6K^2 + \frac{3}{2}a_1^2) + 60K\Lambda(\mu + 2\alpha)\big]\Big\} ,
\end{aligned}
\tag{4.38}
$$

$$
\begin{aligned}
\gamma' = &\, 4\sigma + \frac{1}{2\bar{\omega}_1}\big[3\mu + 4\alpha\big] + \frac{\delta}{2a_1\bar{\omega}_1}\Lambda cos\gamma \\
&+ \frac{1}{a_1\bar{\omega}_1}\Big\{g_3\big[\frac{3}{2}\delta(K + \Lambda)(a_1 + \Lambda cos\gamma) + 2(3\mu + 5\alpha)(\Lambda^2 cos\gamma + a_1 K)\big] \\
&+ g_4\big[3\delta(K^2 a_1 + 2K\Lambda a_1 + 2\Lambda^2 a_1 + \frac{1}{4}a_1^3 + \Lambda(2K\Lambda + \frac{4}{3}\Lambda^2 + K^2 \\
&+ \frac{3}{4}a_1^2)cos\gamma) + 15(\mu + 2\alpha)(2K\Lambda^2 cos\gamma + a_1 K^2 + 2a_1\Lambda^2 + \frac{1}{4}a_1^3)\big]\Big\} .
\end{aligned}
\tag{4.39}
$$

After setting the derivatives equal to zero, one can solve for the steady-state solutions, $a_1' = \gamma' = 0$. The equations predicting the amplitude-frequency response are

$$
\sigma = \frac{-1}{4a_1\bar{\omega}_1}(A_1 a_1^3 + B_1 a_1^2 + C_1 a_1 + D_1) , \tag{4.40}
$$

where

$$
\begin{aligned}
A_1 = &\frac{3}{4}g_4(\delta + 5\mu + 10\alpha) , \\
B_1 = &\frac{9}{4}\delta g_4 \Lambda \cos\gamma , \\
C_1 = &\frac{3}{2}\mu + 2\alpha + g_3\big[\frac{3}{2}\delta(\Lambda + K) + 2K(3\mu + 5\alpha)\big] \\
&+ g_4\big[3\delta(K^2 + 2\Lambda^2 + 2K\Lambda) + 15(\mu + 2\alpha)(K^2 + 2\Lambda^2)\big] , \\
D_1 = &\, \Lambda \cos\gamma\Big\{\frac{1}{2}\delta + g_3\big[\frac{3}{2}\delta(\Lambda + K) + 2\Lambda(3\mu + 5\alpha)\big] \\
&+ g_4\big[\delta(3K^2 + 4\Lambda^2 + 6K\Lambda) + 30K\Lambda(\mu + 2\alpha)\big]\Big\} ,
\end{aligned}
\tag{4.41}
$$

and

$$
a_1 = \frac{-B_2 \pm \sqrt{B_2^2 - 4A_2 C_2}}{2A_2} , \tag{4.42}
$$

where

$$
\begin{aligned}
A_2 =& \frac{3\delta g_4 \Lambda}{4\bar{\omega}_1} \sin\gamma \ , \\
B_2 =& \frac{-b}{2} \ , \\
C_2 =& \frac{\Lambda \sin\gamma}{\bar{\omega}_1} \Big\{ \frac{1}{2}\delta + g_3 \big[\frac{3}{2}\delta(\Lambda + K) + 2\Lambda(3\mu + 5\alpha) \big] \\
& + g_4 \big[\delta(3K^2 + 4\Lambda^2 + 6K\Lambda) + 30\Lambda K(\mu + 2\alpha) \big] \Big\} \ .
\end{aligned}
\tag{4.43}
$$

4.7 Electrostatic Reduced Order Model

This electrostatic ROM is valid for MEMS circular plates with the gap distance greater than one micron, $d > 10^{-6}$m. ROM, if enough number of modes of vibration included, gives accurate results for both weak and strong nonlinearities. The electrostatic ROM includes only the electrostatic force, so no Casimir or van der Waals forces are present, see Eq. (4.3). Therefore the differential equation of motion Eq. (4.3), has the Casimir and van der Waals parameters α and μ set to zero. This equation is then multiplied by $(1-u)^2$ in order to have no denominator in the differential equation. So Eq. (4.3) becomes

$$
\ddot{u}(1 - 2u + u^2) + \dot{u}b(1 - 2u + u^2) + (1 - 2u + u^2)P[u] = \delta \cos^2 \Omega t \ , \tag{4.44}
$$

where $P[u]$ is given by Eq. (4.4). The solution u, which describes the deflection of the plate, is written in terms of the first N dimensionless modeshapes of the circular plate as follows:

$$
u(r,t) = \sum_{i=1}^{N} u_i(t)\phi_i(r) \ , \tag{4.45}
$$

where $\phi_i(r)$ are the dimensionless modeshapes and $u_i(t)$ are time functions to be determined. Substituting Eqs. (4.45) and (4.7) into Eq. (4.44), it results

$$
\begin{aligned}
& \sum_{i=1}^{N} \ddot{u}_i \Big[\phi_i - 2\sum_{j=1}^{N} u_j\phi_i\phi_j + \sum_{j,k=1}^{N} u_j u_k \phi_i \phi_j \phi_k \Big] \\
& + b\sum_{i=1}^{N} \dot{u}_i \Big[\phi_i - 2\sum_{j=1}^{N} u_j\phi_i\phi_j + \sum_{j,k=1}^{N} u_j u_k \phi_i \phi_j \phi_k \Big] \\
& + \sum_{i=1}^{N} u_i\omega_i^2 \Big[\phi_i - 2\sum_{j=1}^{N} u_j\phi_i\phi_j + \sum_{j,k=1}^{N} u_j u_k \phi_i \phi_j \phi_k \Big] = \delta \cos^2 \Omega t \ ,
\end{aligned}
\tag{4.46}
$$

where N is the number of modes of vibration used in the ROM. Using Galerkin procedure, Eq. (4.46) is multiplied by r and ϕ_n and then integrated from 0 to 1, i.e.

Eq. (4.46) is transformed by the following operator

$$\int_0^1 \bullet r\phi_n(r)dr \ . \tag{4.47}$$

One should mention that *n* = 1,2,...,*N*, so a system of *N* second-order differential equation is obtained, where the *h*-coefficients are given by Eq. (4.48). Since this work includes three ROMs, i.e. electrostatic ROM which includes only the electrostatic force but no Casimir and van der Waals, Casimir ROM which includes the electrostatic and Casimir forces, and van der Waals ROM which includes electrostatic and van der Waals forces, *h*-coefficents are given by Eq. (4.48) for all three cases. The electrostatic ROM only uses the first four, h_n, h_{ni}, h_{nij},and h_{nijk}, the van der Waals ROM uses h_n, h_{ni}, h_{nij}, h_{nijk}, and h_{nijkl}, and the Casimir model uses h_n, h_{ni}, h_{nij}, h_{nijk}, h_{nijkl}, and h_{nijklm},

$$\begin{gathered} h_n = \int_0^1 r\phi_n dr \ , \ \ h_{ni} = \int_0^1 r\phi_n\phi_i dr \ , \ \ h_{nij} = \int_0^1 r\phi_n\phi_i\phi_j dr \ , \\ h_{nijk} = \int_0^1 r\phi_n\phi_i\phi_j\phi_k dr \ , \ \ h_{nijkl} = \int_0^1 r\phi_n\phi_i\phi_j\phi_k\phi_l dr \ , \\ h_{nijklm} = \int_0^1 r\phi_n\phi_i\phi_j\phi_k\phi_l\phi_m dr \ . \end{gathered} \tag{4.48}$$

New variables y_k are introduced as follows:

$$y_{2k-1} = u_k, y_{2k} = \dot{u}_k, \dot{y}_{2k} = \ddot{u}_k, k = 1, 2 \ldots N \tag{4.49}$$

With these new variables the system of N second-order differential equations is transformed into a system of $2N$ first-order differential equations given by

$$\begin{cases} \dot{y}_{2n-1} = y_{2n} \\ \displaystyle\sum_{i=1}^{N} \dot{y}_{2i} A_{ni} = -b \sum_{i=1}^{N} y_{2i} A_{ni} - \sum_{i=1}^{N} \omega_i^2 \cdot y_{2i-1} A_{ni} + \delta h_n \cos^2 \Omega t \end{cases} \tag{4.50}$$

where $n = 1, 2, \ldots, N$ and A_{ni} are as follows

$$A_{ni} = h_{ni} - 2\sum_{j=1}^{N} h_{nij} \cdot y_{2j-1} + \sum_{j,k=1}^{N} h_{nijk} \cdot y_{2j-1} \cdot y_{2k-1} \ . \tag{4.51}$$

In order to predict the amplitude-frequency response (bifurcation diagram) of the superharmonic resonance of second-order of the MEMS circular plate, the continuation and bifurcation method (AUTO 07p software package) is used to solve Eqs. (4.50). Also, same Eqs. (4.50) are numerically integrated using Matlab in order to predict time responses of the MEMS circular plate.

4.8 Casimir Reduced Order Model

Casimir ROM is valid for NEMS circular plates with the gap distance d less than one micron and greater than 100 nanometers, $100 \times 10^{-9}\text{m} < d < 10^{-6}\text{m}$. The governing equation of the Casimir ROM is given by

$$\begin{aligned}&\ddot{u}(1-4u+6u^2-4u^3+u^4)+\dot{u}b(1-4u+6u^2-4u^3+u^4)\\&+(1-4u+6u^2-4u^3+u^4)P[u]=(1-2u+u^2)\delta\cos^2\Omega t+\alpha\ ,\end{aligned} \tag{4.52}$$

where Eq. (4.3) was multiplied by $(1-u)^4$. The van der Waals parameter was set to zero. $P[u]$ is given by Eq.(4.4). Substituting Eq. (4.45) and Eq. (4.7) into Eq.(4.52), it results

$$\begin{aligned}&\sum_{i=1}^{N}\ddot{u}_i\Big[\phi_i-4\sum_{j=1}^{N}u_j\phi_i\phi_j+6\sum_{j,k=1}^{N}u_ju_k\phi_i\phi_j\phi_k\\&-4\sum_{j,k,l=1}^{N}u_ju_ku_l\phi_i\phi_j\phi_k\phi_l+\sum_{j,k,l,m=1}^{N}u_ju_ku_lu_m\phi_i\phi_j\phi_k\phi_l\phi_m\Big]\\&+b\sum_{i=1}^{N}\dot{u}_i\Big[\phi_i-4\sum_{j=1}^{N}u_j\phi_i\phi_j+6\sum_{j,k=1}^{N}u_ju_k\phi_i\phi_j\phi_k\\&-4\sum_{j,k,l=1}^{N}u_ju_ku_l\phi_i\phi_j\phi_k\phi_l+\sum_{j,k,l,m=1}^{N}u_ju_ku_lu_m\phi_i\phi_j\phi_k\phi_l\phi_m\Big]\\&+\sum_{i=1}^{N}u_i\omega_i^2\Big[\phi_i-4\sum_{j=1}^{N}u_j\phi_i\phi_j+6\sum_{j,k=1}^{N}u_ju_k\phi_i\phi_j\phi_k\ldots\\&\ldots-4\sum_{j,k,l=1}^{N}u_ju_ku_l\phi_i\phi_j\phi_k\phi_l+\sum_{j,k,l,m=1}^{N}u_ju_ku_lu_m\phi_i\phi_j\phi_k\phi_l\phi_m\Big]\\&=\delta\Big[1-2\sum_{i=1}^{N}u_i\phi_i+\sum_{i,j=1}^{N}u_iu_j\phi_i\phi_j\Big]\cos^2\Omega t+\alpha\end{aligned} \tag{4.53}$$

where *N* is the number of modes of vibration in the ROM. Multiplying Eq. (4.53) by Eq. (4.47) and using Eqs. (4.48) and (4.49) it results

$$\begin{cases} \dot{y}_{2n-1} = y_{2n} \\ \sum_{i=1}^{N} \dot{y}_{2i} B_{ni} = -b \sum_{i=1}^{N} y_{2i} B_{ni} - \sum_{i=1}^{N} \omega_i^2 \cdot y_{2i-1} B_{ni} \\ + \delta \left[h_n - 2 \sum_{i=1}^{N} h_{ni} \cdot y_{2i-1} + \sum_{i,j=1}^{N} h_{nij} \cdot y_{2i-1} \cdot y_{2j-1} \right] cos^2 \Omega t + \alpha h_n \end{cases} \tag{4.54}$$

where $n = 1, 2, \ldots, N$ and B_{ni} are as follows:

$$\begin{aligned} B_{ni} = & h_{ni} - 4 \sum_{j=1}^{N} h_{nij} \cdot y_{2j-1} + 6 \sum_{j,k=1}^{N} h_{nijk} \cdot y_{2j-1} \cdot y_{2k-1} \\ & - 4 \sum_{j,k,l=1}^{N} h_{nijkl} \cdot y_{2j-1} \cdot y_{2k-1} \cdot y_{2l-1} \\ & + \sum_{j,k,l,m=1}^{N} h_{nijklm} \cdot y_{2j-1} \cdot y_{2k-1} \cdot y_{2l-1} \cdot y_{2m-1} \, . \end{aligned} \tag{4.55}$$

The amplitude-frequency response of the superharmonic resonance of second-order is predicted using continuation and bifurcation (AUTO 07p software package) to solve Eqs. (4.54). Also, time responses are predicted through numerical integration of Eqs. (4.54) using Matlab.

4.9 Van der Waals Reduced Order Model

Van der Waals ROM is valid for NEMS circular plates with the gap distance d less than 50 nanometers, $d < 50 \times 10^{-9}$m. The ROM takes into consideration the effect of van der Waals forces. Hence in Eq. (4.3) the Casimir parameter α is set to zero. Multiplying both sides by $(1-u)^3$ as it is the largest denominator, and expanding, it results

$$\begin{aligned} & \ddot{u}(1 - 3u + 3u^2 - u^3) + \dot{u}b(1 - 3u + 3u^2 - u^3) + (1 - 3u + 3u^2 - u^3)P[u] \\ & = \delta(1-u)\cos^2 \Omega t + \mu \, . \end{aligned} \tag{4.56}$$

Substituting Eq.(4.45) and Eq.(4.7) into Eq.(4.56), it results

$$\sum_{i=1}^{N}\ddot{u}_i\left[\phi_i-3\sum_{j=1}^{N}u_j\phi_i\phi_j+3\sum_{j,k=1}^{N}u_ju_k\phi_i\phi_j\phi_k-\sum_{j,k,l=1}^{N}u_ju_ku_l\phi_i\phi_j\phi_k\phi_l\right]$$
$$+b\sum_{i=1}^{N}\dot{u}_i\left[\phi_i-3\sum_{j=1}^{N}u_j\phi_i\phi_j+3\sum_{j,k=1}^{N}u_ju_k\phi_i\phi_j\phi_k-\sum_{j,k,l=1}^{N}u_ju_ku_l\phi_i\phi_j\phi_k\phi_l\right]$$
$$+\sum_{i=1}^{N}u_i\omega_i^2\left[\phi_i-3\sum_{j=1}^{N}u_j\phi_i\phi_j+3\sum_{j,k=1}^{N}u_ju_k\phi_i\phi_j\phi_k-\sum_{j,k,l=1}^{N}u_ju_ku_l\phi_i\phi_j\phi_k\phi_l\right]$$
$$=\delta\left[1-\sum_{i=1}^{N}u_i\phi_i\right]cos^2\Omega t+\mu\ . \tag{4.57}$$

where N is the number of modes of vibration in the ROM. Multiplying (4.57) by Eq. (4.47), and using (4.48) and (4.49), it results

$$\begin{cases}\dot{y}_{2n-1}=y_{2n}\\ \sum_{i=1}^{N}\dot{y}_{2i}C_{ni}=-b\sum_{i=1}^{N}y_{2i}C_{ni}-\sum_{i=1}^{N}\omega_i^2\cdot y_{2i-1}C_{ni}\\ +\delta\left[h_n-\sum_{i=1}^{N}h_{ni}\cdot y_{2i-1}\right]\cos^2\Omega t+\mu h_n\ ,\end{cases} \tag{4.58}$$

where *n* = 1,2,...,*N* and C_{ni} are given by

$$C_{ni}=h_{ni}-3\sum_{j=1}^{N}h_{nij}\cdot y_{2j-1}+3\sum_{j,k=1}^{N}h_{nijk}\cdot y_{2j-1}\cdot y_{2k-1}$$
$$-\sum_{j,k,l=1}^{N}h_{nijkl}\cdot y_{2j-1}\cdot y_{2k-1}\cdot y_{2l-1}\ . \tag{4.59}$$

The system of $2N$ first-order differential equations is solved numerically using AUTO 07p for predicting the bifurcation diagram, and numerically integrated using Matlab's built-in solver *ode15s* for time responses.

4.10 Numerical Simulations

4.10.1 Electrostatic Model of Microelectromechanical Systems Clamped Circular Plates

Figure 4.2 shows the amplitude-frequency response in the case of MEMS, i.e. the gap distance, $d > 10^{-6}$m. The horizontal axis represents the detuning frequency σ, where at σ = 0, the *AC* frequency is exactly one fourth of the first dimensionless natural frequency of the MEMS clamped circular plate. The vertical axis represents the dimensionless amplitude at the center of the plate *Umax*. The stable branches are denoted by solid lines, and the unstable branches by dashed lines. Figure 4.2 shows the predictions of three methods, 1) one term ROM of second-order model of hard excitations (2TnE), and 25th degree Taylor polynomial to approximate the electrostatic force, that was solved using MMS in order to predict the amplitude-frequency response, 2) a six term (6T) ROM numerically integrated using Matlab that predicted time responses, and 3) six term (6T) ROM solved using the continuation and bifurcation method (AUTO) that predicted the amplitude-frequency response. These methods predict the existence of saddle-node bifurcation point A. As the frequency is swept up, the 6T ROM AUTO predicts that the steady state amplitude increases along branch 1 until the system reaches point A, where it experiences a jump phenomenon, the amplitude jumping up from point A to branch 3. If the frequency continues to be swept up the steady-state amplitudes decreases along branch 3. If the frequency is swept down, the amplitude increases along branch 3 until it reaches point C. At this point the system loses stability and experiences pull-in, i.e., the dimensionless amplitude reaches the value of 1. In the case of constant frequency, and initial amplitude above branch 3, the amplitudes settle on the stable branch 3. For frequencies between σ_B and σ_C and initial amplitudes above branch 2, the MEMS circular plate experiences pull-in. For frequencies less than σ_B, regardless the value of the initial amplitude, the amplitudes settle on the stable branch 1. For any initial amplitude bellow branch 2, and for frequencies between σ_B and σ_A, the amplitudes settle on the stable branch 1. For any initial amplitude above branch 2, and frequencies greater than σ_C, the amplitudes settle on branch 3. One should mention that for zero initial amplitude and frequencies less than σ_A, the amplitudes settle one branch 1. Figures 4.3 and 4.4 show predicted time responses resulted from numerical integration of the 6T ROM. They are in agreement with the predictions resulted from continuation and bifurcation of 6T ROM AUTO. Figures 4.3a and 4.3c for $\sigma = -0.08$, and Figs. 4.4a and 4.4c for $\sigma = -0.12$, show time responses for initial amplitudes $U_0 = 0.4$ and $U_0 = 0.8$. One can notice that depending on the initial amplitude U_0, the amplitude settles either on branch 3 or 1, which is in agreement with AUTO predictions. Figures 4.3b and 4.3d show time responses from zero initial amplitudes $U_0 = 0.0$ and frequencies greater than σ_A. The amplitudes settle on branch 3. Figures 4.4a and 4.4b do not contradict the existence of end points B and C. Figures 4.4b and 4.4d show time responses from high initial amplitudes U_0 = 0.8 and frequencies less than σ_B. For both time responses the amplitudes settle on

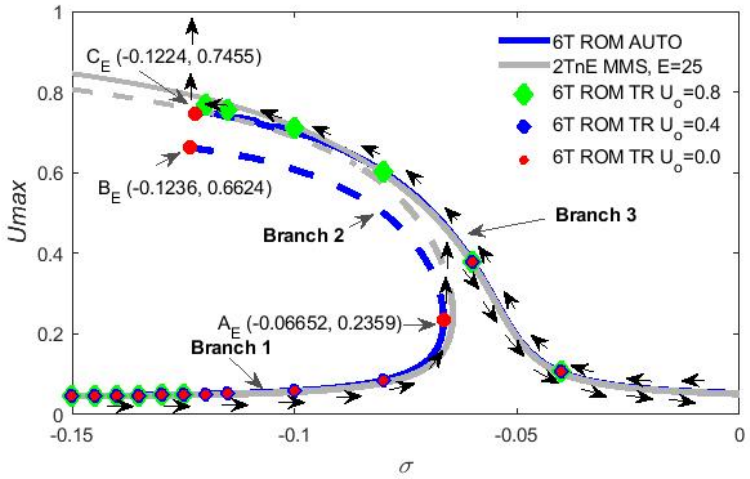

Fig. 4.2 Amplitude-frequency response using Electrostatic 6T ROM and Electrostatic 2TnE MMS $E = 25$, $\delta = 4$, $b = 0.025$, $\alpha = 0$, $\mu = 0$, where E is the degree of the electrostatic Taylor polynomial in MMS

branch 1. This is in agreement with 6T ROM AUTO predictions. Figure 4.5 shows the effect of increasing the number of modes of vibration (terms) in ROM. ROMs with two terms, three terms, four terms, five terms. and six terms are included. One can notice that there is no significant difference between ROMs with five terms, and six terms. This is the reason the 6T ROM is used in this research. Figure 4.6 illustrates the convergence of MMS predictions with respect to the degree E of the Taylor polynomial approximating the electrostatic force. The one term no epsilon model (1TnE) is also compared to the two term no epsilon model (2TnE). As the number of terms in the Taylor polynomial for the 2TnE model increases, the upper part of the branches moves to lower amplitudes, toward AUTO predictions. As mentioned before, MMS cannot predict the end points of the amplitude-frequency response. Additionally, MMS is limited to good results in lower amplitudes, amplitudes less than 0.2 of the gap. Overall, the change in lower amplitudes with increasing the degree of Taylor polynomial is not significant. A polynomial of degree 25 was deemed sufficient, as no significant changes in the predictions of 2TnE for degrees of Taylor polynomial great than $E = 25$ were observed. However, MMS is not reliable in predicting higher steady-state amplitudes.

Figure 4.7 shows the effect of voltage parameter on the amplitude-frequency response using two methods, 6T ROM AUTO and MMS 2TnE. For a smaller voltage of δ = 2, both methods show only one branch with a relatively small peak amplitude and rather a linear behavior. MMS is in agreement with AUTO for amplitudes less than 0.2 of the gap, regardless of the voltage values. As the voltage increases from δ = 2 to δ = 3 the peak amplitude increases. As the voltage increases to δ = 4 the three

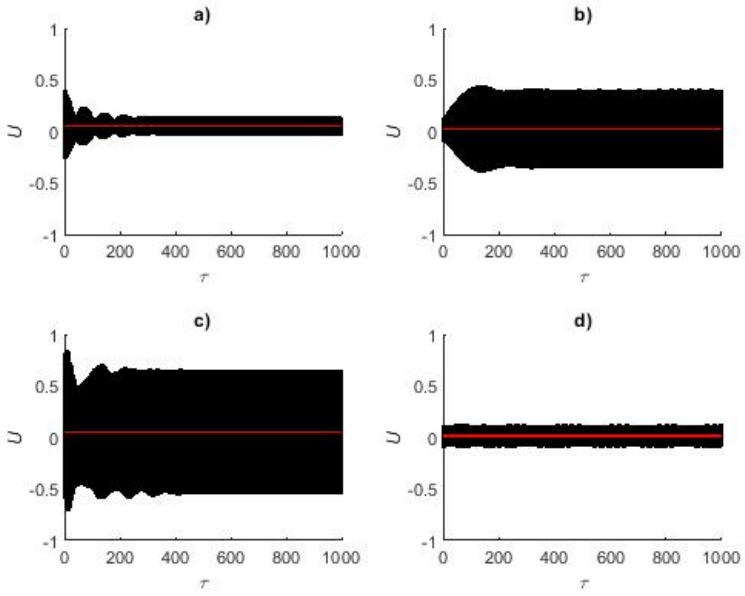

Fig. 4.3 Electrostatic 6T ROM Time Responses: $\delta = 4$, $b = 0.025$, $\alpha = 0$, $\mu = 0$: a) $U_0 = 0.4$, $\sigma = -0.08$, b) $U_0 = 0.0$, $\sigma = -0.06$, c) $U_0 = 0.8$, $\sigma = -0.08$, d) $U_0 = 0.0$, $\sigma = -0.04$

branches 1,2, and 3 are born showing a consistent nonlinear behavior. The existence of the unstable branch 2 explains the fact that for different initial amplitudes the system can settle to either a small amplitude on branch 1, or a larger amplitude on branch 3. Also in the case δ = 4 branches 2 and 3 have end points predicting the existence of pull-in phenomenon for frequencies between σ_B and σ_C.

Figure 4.8 shows the effect of damping on the amplitude-frequency response. This effect is investigated at high voltage δ = 4. In a similar fashion to the effect of the voltage on the amplitude-frequency response, MMS predictions are in agreement with 6T ROM AUTO for amplitudes lower than 0.2 of the gap. For damping parameter values b = 0.035 and b = 0.025, the difference between MMS and 6T ROM AUTO is quite significant in large amplitudes. Significant differences of the two methods, MMS and 6T ROM AUTO, are seen in the case of smaller damping b = 0.025. For higher damping b = 0.045, the peak amplitudes reduce, as well as the difference between MMS and 6T ROM AUTO.

Figure 4.9 shows the voltage bias using 6T ROM AUTO. This bias is directly related to Fig. 4.2. As shown in Fig. 4.9, the bias is at less than 5.5 $\%$ of the gap distance d. This suggests that the bias does not have a significant influence on the behavior of the system.

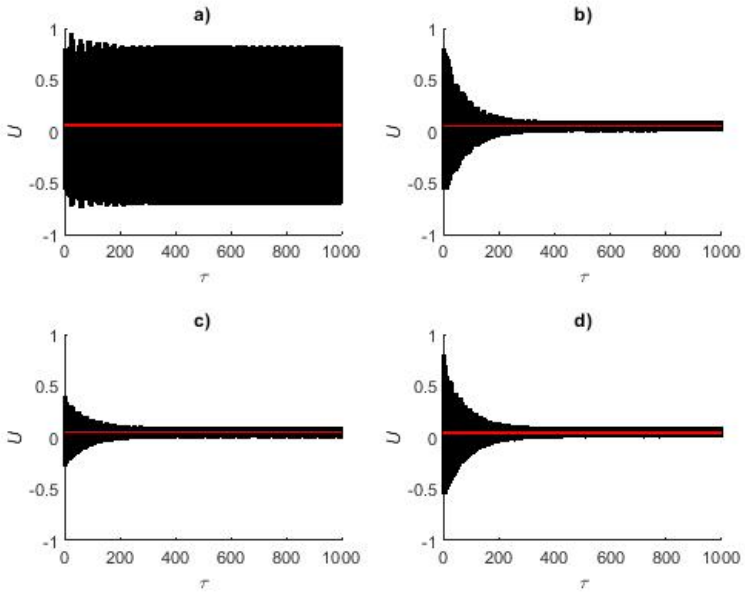

Fig. 4.4 Electrostatic 6T ROM Time Responses: $\delta = 4$, $b = 0.025$, $\alpha = 0$, $\mu = 0$: a) $U_0 = 0.8$, $\sigma = -0.12$, b) $U_0 = 0.8$, $\sigma = -0.125$, c) $U_0 = 0.4$, $\sigma = -0.12$, d) $U_0 = 0.8$, $\sigma = -0.15$

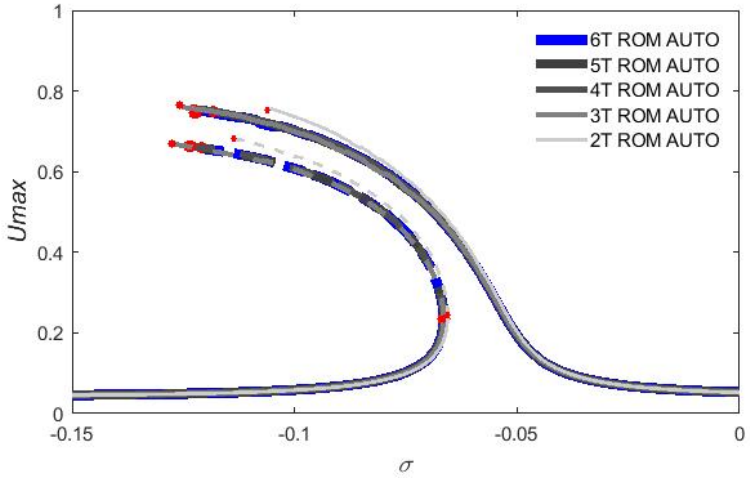

Fig. 4.5 Effect of the number of modes of vibration N in ROM on the amplitude-frequency response: $\delta = 4$, $b = 0.025$, $\alpha = 0$, $\mu = 0$

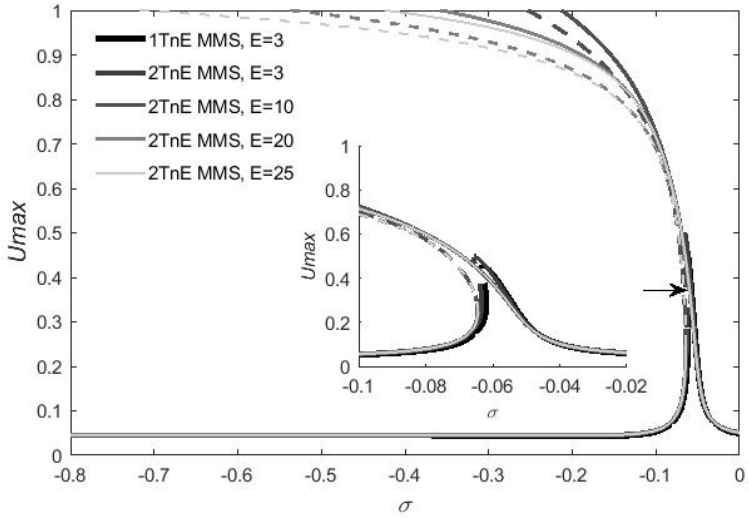

Fig. 4.6 Effect of E, the degree of the Taylor polynomial approximating the electrostatic force in MMS, on the amplitude-frequency responses $\delta = 4$, $b = 0.025$, $\alpha = 0$, $\mu = 0$

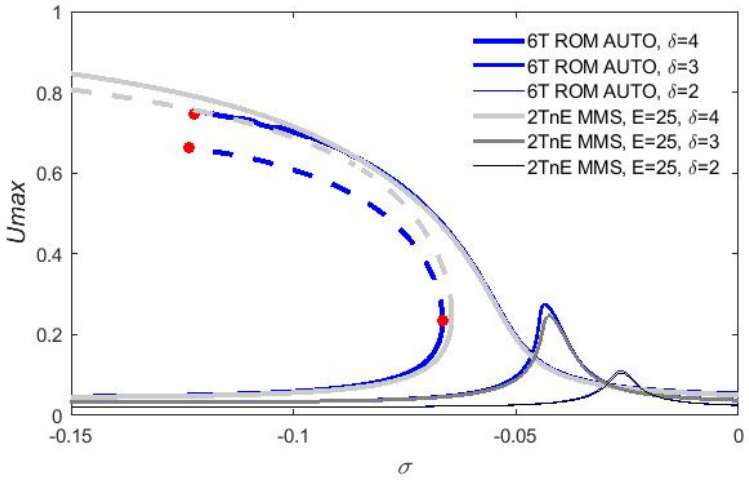

Fig. 4.7 Effect of δ, the dimensionless voltage parameter, on the amplitude-frequency response using electrostatic 6T ROM AUTO, and electrostatic 2TnE MMS polynomial of $E = 25$ degree: $b = 0.025$, $\alpha = 0$, $\mu = 0$

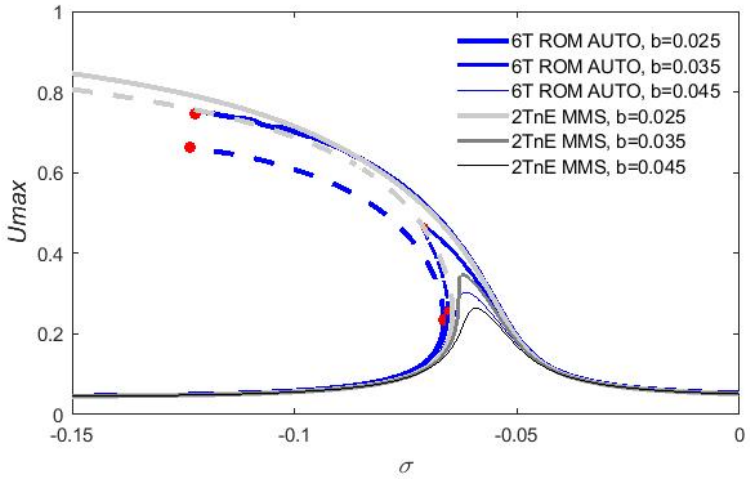

Fig. 4.8 Effect of b, the dimensionless damping parameter, on the amplitude-frequency response using Electrostatic 6T ROM AUTO and Electrostatic 2TnE MMS polynomial of $E = 25$ degree, $\delta = 4$, $\alpha = 0$, $\mu = 0$

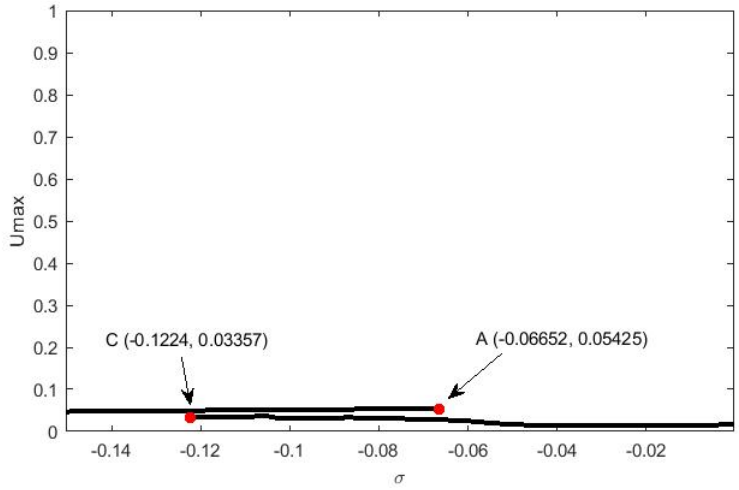

Fig. 4.9 Voltage Bias using 6T ROM AUTO, $\delta = 4$, $b = 0.025$

4.10.2 Casimir Force Effect on Nanoelectromechanical Systems Plates

Figure 4.10 shows the effect of the Casimir parameter α on the amplitude-frequency response. Increasing the Casimir parameter α leads to an increase of the softening effect, a decrease of the steady-state amplitudes for a given frequency σ in the resonance zone, and/or a shifting of the amplitude-frequency response to lower frequencies. MMS predictions are in agreement with 6T ROM AUTO for amplitudes less than 0.2 of the gap, if $\alpha = 0$, and amplitudes less than 0.1 of the gap if $\alpha = 0.2$. This is consistent with the fact that MMS is valid for weak nonlinearities and small amplitudes. The increase of the Casimir parameter shifts the bifurcation point A and the endpoints B and C to lower frequencies. The bifurcation point A is significantly shifted to lower frequencies. Figure 4.11 shows the amplitude-frequency response

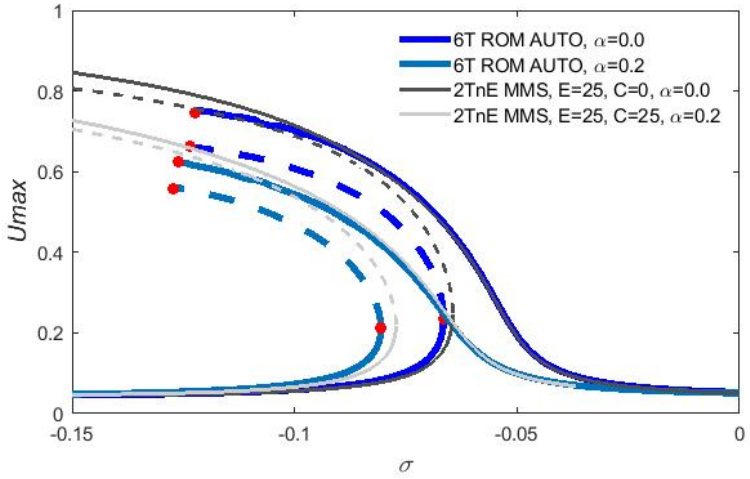

Fig. 4.10 Effect of α, the dimensionless Casimir parameter, on the amplitude-frequency response using electrostatic and Casimir 6T ROM AUTO and 2TnE MMS polynomials of 25th degree. $\delta = 4$, $b = 0.025$, $\mu = 0$, E is the degree of the electrostatic Taylor polynomial, C is the degree of the Casimir Taylor polynomial. It should be noted that if $\alpha = 0$, then the model used was the electrostatic model.

in the case of Casimir effect, $\alpha = 0.2$, using 6T ROM AUTO. Also time responses using 6T ROM are shown in Figs. 4.12 and 4.13. As one can see, the two methods are in agreement. Figure 4.12a shows a time response with an initial amplitude $U_0 = 0.2$ and detuning frequency $\sigma = -0.085$. This point is towards the left of bifurcation point A, and moves away from the unstable branch 2 towards the stable branch 1. Figure 4.12b shows a time response from $U_0 = 0.0$ and $\sigma = -0.08$ that settles on branch 3. This is not in disagreement with the existence of bifurcation point A. For

the same $\sigma = -0.085$ as Fig. 4.12a, the time response in Fig. 4.12c starts now from a $U_0 = 0.7$ and the amplitude settles on stable branch 3. Figure 4.12d shows a point in the lower amplitudes of branch 3. Figures 4.13a and 4.13c show time responses for a frequency $\sigma = -0.125$ and initial amplitudes, $U_0 = 0.7$ and $U_0 = 0.4$, respectively. The initial amplitude $U_0 = 0.4$ is below the unstable branch 2, so the amplitude settles on branch 1. In the case of $U_0 = 0.7$, which is above branch 3, the amplitude settles on branch 3. Figures 4.13b and 4.13d show time responses from initial amplitude, $U_0 = 0.7$ and frequencies $\sigma = -0.13$ and $\sigma = -0.15$, for which the amplitudes settle on branch 1. Figure 4.14 shows the effect of the degree

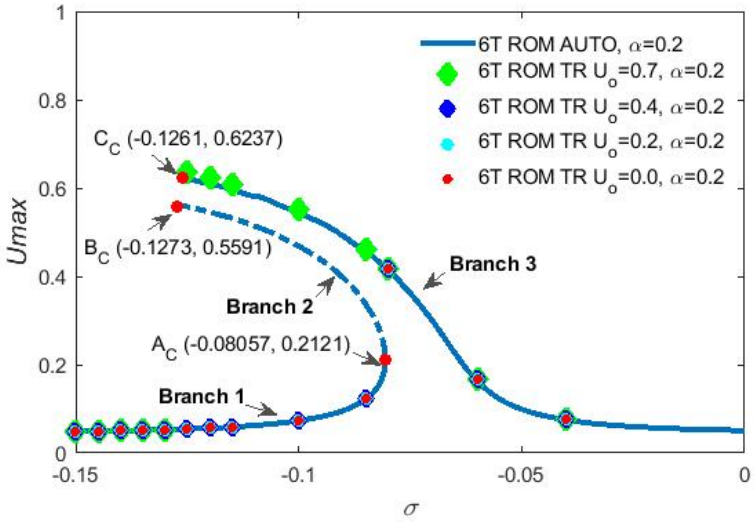

Fig. 4.11 Amplitude-frequency response using Casimir 6T ROM AUTO and Casimir 6T ROM Time Responses, $\delta = 4$, $b = 0.025$, $\alpha = 0.2$, $\mu = 0$

of Taylor polynomial approximating the Casimir force, E and C are the degrees of Taylor polynomials approximating the electrostatic and Casimir forces, respectively. The 2TnE model is also compared with the 1TnE model. The 2TnE predicts a stronger softening effect, which is more accurate. Furthermore, 1TnE MMS model does not predict the existence of the three branches in higher amplitudes. In order to see the effect of increasing the degree of the Casimir Taylor polynomial, the 2TnE model used a 25th degree electrostatic Taylor polynomial. Overall, increasing the degree of the Casimir Taylor polynomial shows a similar behavior to that of the electrostatic Taylor polynomial effect, in which the branches show a stronger softening effect. As there was no significant difference in the amplitude-frequency response between Casimir Taylor polynomials of 20th and 25th degree, the 25th degree Casimir Taylor polynomial was sufficient.

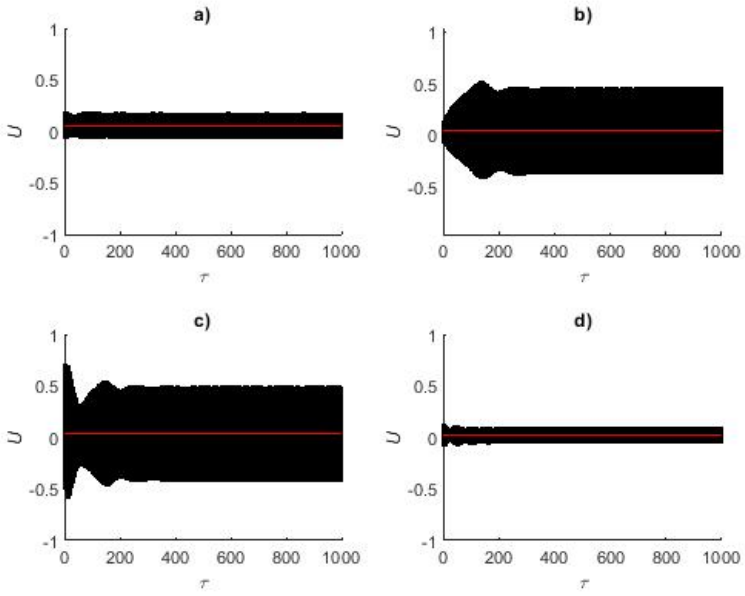

Fig. 4.12 Casimir 6T ROM Time Responses, $\delta = 4$, $b = 0.025$, $\alpha = 0.2$, $\mu = 0$: a) $U_0 = 0.2$, $\sigma = -0.085$, b) $U_0 = 0.0$, $\sigma = -0.08$, c) $U_0 = 0.7$, $\sigma = -0.085$, d) $U_0 = 0.0$, $\sigma = -0.04$

4.10.3 Van der Waals Force Effect on Nanoelectromechanical Systems Plates

Figure 4.15 shows the effect of the van der Waals parameter on the amplitude-frequency response using 6T ROM AUTO and 2TnE MMS. The van der Waals parameter effect on the amplitude-frequency response is similar to the effect of Casimir parameter, it causes a reduction of the higher amplitudes for both MMS and ROM predictions. Furthermore, it also causes a shifting of stable and unstable branches towards lower frequencies, which can also be seen in the case of saddle-node bifurcation point A. The lower amplitudes remain unaffected outside the resonance zone. Figure 4.16 shows the amplitude-frequency response to include van der Waals forces. Both 6T ROM AUTO and 6T ROM time responses are included. Time response with $U_0 = 0.25$ and $\sigma = -0.08$ settles to an amplitude on the stable branch 1, Fig. 4.17a. Time response with $U_0 = 0.0$ and $\sigma = -0.075$ settles to an amplitude on branch 3, Fig. 4.17b. Figure 4.17c shows a time response from higher initial amplitude $U_0 = 0.75$ and $\sigma = -0.08$, that settles to an amplitude on branch 3. Figure 4.17d shows a time response from $U_0 = 0.0$ and $\sigma = -0.04$, which settles to an amplitude on branch 3. Figures 4.18a and 4.18c show time responses at $\sigma = -0.12$ from different initial amplitudes. Figure 4.18a starts from $U_0 = 0.75$

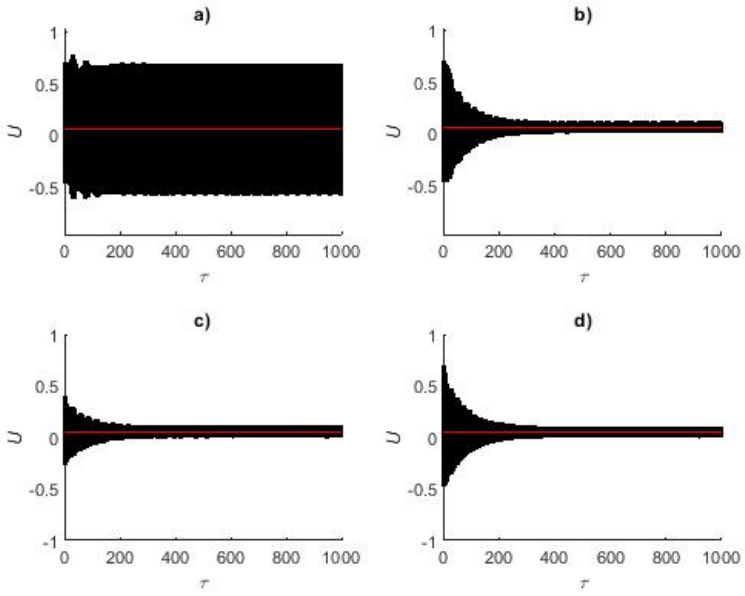

Fig. 4.13 Casimir 6T ROM Time Responses, $\delta = 4$, $b = 0.025$, $\alpha = 0.2$, $\mu = 0$: a) $U_0 = 0.7$, $\sigma = -0.125$, b) $U_0 = 0.7$, $\sigma = -0.13$, c) $U_0 = 0.4$, $\sigma = -0.125$, d) $U_0 = 0.7$, $\sigma = -0.15$

and settles on stable branch 3, while 4.18c starts at $U_0 = 0.25$ and settles on stable branch 1. Figure 4.18b shows a point from a higher initial amplitude $U_0 = 0.75$ and at a frequency $\sigma = -0.125$, which is lower than the end points B and C that settles to an amplitude on the stable branch 1. This is not in disagreement with the endpoints predicted by AUTO. Figure 4.18d shows behavior similar to that of Fig. 4.18b. Figure 4.19 shows the effect of the degree of the Taylor polynomial approximating the van der Waals force, where E and V are the degrees of the Taylor polynomials approximating the electrostatic force and the van der Waals force, respectively. As in the Casimir case and the Electrostatic case, the 2tnE model of the van der Waals case is more accurate than the 1TnE. Therefore the Taylor polynomials in the 2TnE model are used. The 1TnE MMS model also shows no splitting of the branches 2 and 3, unlike the 2TnE. As the degree of the Taylor polynomial increases, the 2TnE MMS model shows a behavior similar to that predicted by the 6T ROM AUTO. One can notice that there is no significant difference in predictions between $V = 20$ and $V = 25$. Therefore a van der Waals Taylor polynomial of 25th degree has been used.

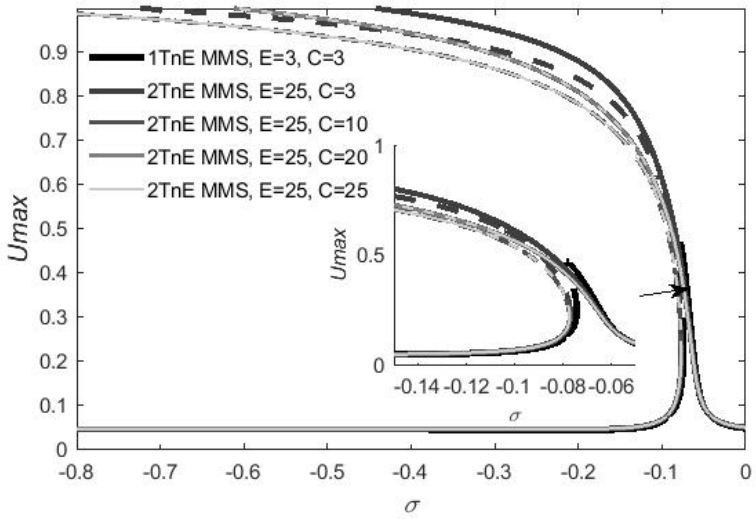

Fig. 4.14 Effect of C, the degree of the Taylor polynomial approximating the Casimir force in MMS, on the amplitude-frequency response using 1TnE MMS $E = 3$ and 2TnE MMS $E = 25$, $\delta = 4$, $b = 0.025$, $\alpha = 0.2$, $\mu = 0$, E is the degree of electrostatic Taylor polynomial, C is the degree of the Casimir Taylor polynomial

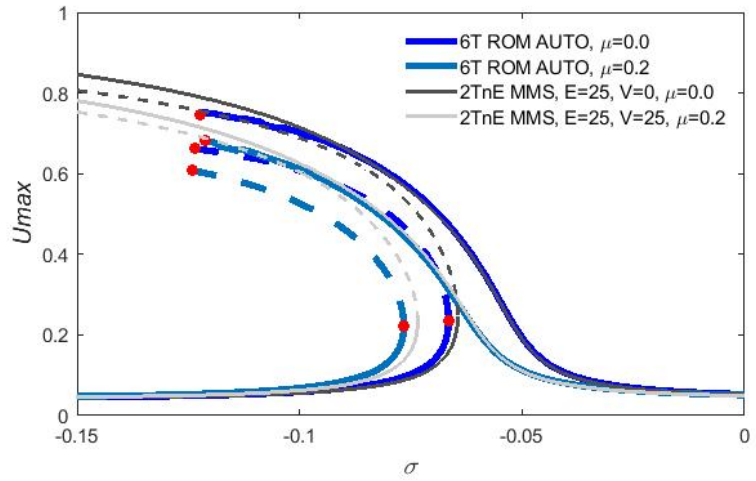

Fig. 4.15 Effect of μ, the dimensionless van der Waals parameter, on the amplitude-frequency response using electrostatic and van der Waals 6T ROM AUTO and 2TnE MMS polynomials of 25th degree, $\delta = 4$, $b = 0.025$, $\mu = 0$, E is the degree of electrostatic Taylor polynomial, V is the degree of the van der Waals Taylor polynomial. It should be noted that if $\mu = 0$, then the model used was the electrostatic model.

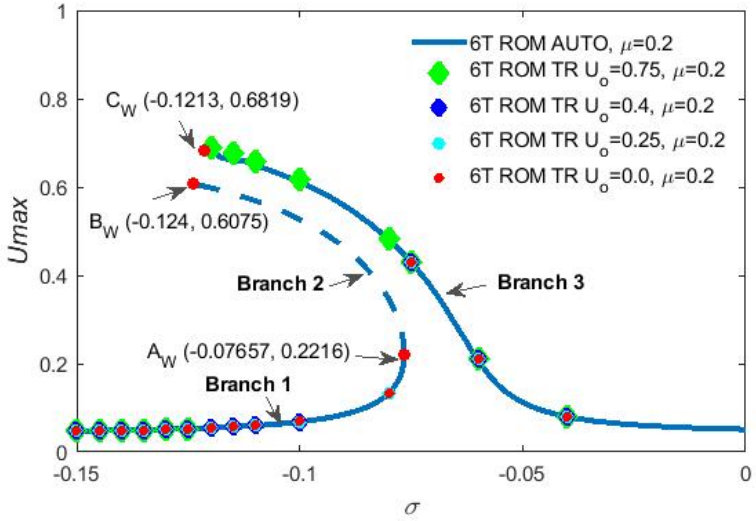

Fig. 4.16 Amplitude-frequency response using van der Waals 6T ROM AUTO and van der Waals 6T ROM Time response, $\delta = 4$, $b = 0.025$, $\alpha = 0$, $\mu = 0.2$

4.10.4 Stability

Figure 4.20 shows points of the amplitude-frequency response that have been tested for stability. The eigenvalues λ_1 and λ_2 of the Jacobian Eq. (4.30) are given in Table 4.7. One can notice that points D, F and G have complex eigenvalues with negative real parts which correspond to stable spiral points. Point E has two real eigenvalues, one positive and one negative, which corresponds to a saddle point, which is unstable.This does not contradict the stability of branches predicted by 6T ROM AUTO.

Table 4.7 Stability testing

Point on Fig. 4.20	a_0	γ_0	σ	λ_1, λ_2
D	0.00580	0.05	-0.11763	-0.01249+0.25708i, -0.01249-0.25708i
E	0.08843	0.8	0.06196	-0.07606, 0.05253
F	0.11703	2.0	-0.05943	-0.01127+0.09531i,-0.01127-0.09531i
G	0.00482	3.1	0.01996	-0.01249+0.30561i,-0.01249-0.30561i

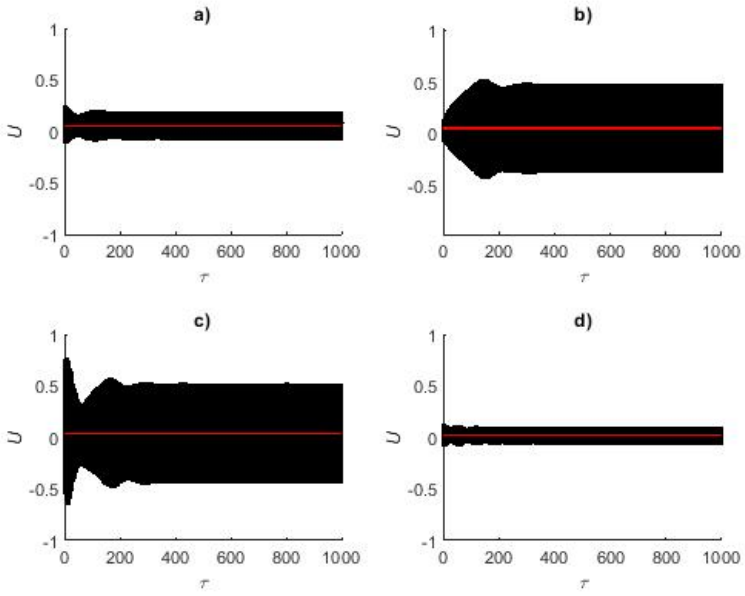

Fig. 4.17 van der Waals 6T ROM Time Responses, $\delta = 4$, $b = 0.025$, $\alpha = 0$, $\mu = 0.2$: a) $U_0 = 0.25$, $\sigma = -0.08$, b) $U_0 = 0.0$, $\sigma = -0.075$, c) $U_0 = 0.75$, $\sigma = -0.08$, d) $U_0 = 0.0$, $\sigma = -0.04$

4.11 Discussion and Conclusions

The novelty of this research consists of predicting the amplitude-frequency response of superharmonic resonance of second-order of electrostatically actuated clamped M/NEMS circular plates to include Casimir and van der Waals effects. Two MMS models of hard excitations have been proposed, and an investigation on the degree of Taylor polynomials approximating the electrostatic, Casimir, and van der Waals forces has been conducted. Several ROMs have been used in this work, and it has been concluded that the ROM using six modes of vibrations (6T) is the most viable method in all amplitudes, lower and higher. The 6T ROM has been solved using AUTO, a software package for continuation and bifurcation, and numerical integration Matlab for time responses. 6T ROM AUTO and 6T ROM time responses were in agreement.

Overall MMS is a fast and easy way to predict the frequency response of clamped circular plate resonators. MMS predicts the lower amplitudes quite well, as it matches those of the 6T ROM. Furthermore, for parameters in which MMS branches are split, the lack of endpoints B and C of branches 2 and 3 in the MMS model is a serious deficiency in predicting the occurrence of pull-in. Also MMS does not necessarily provide very accurate results in high amplitudes and definitely cannot predict B

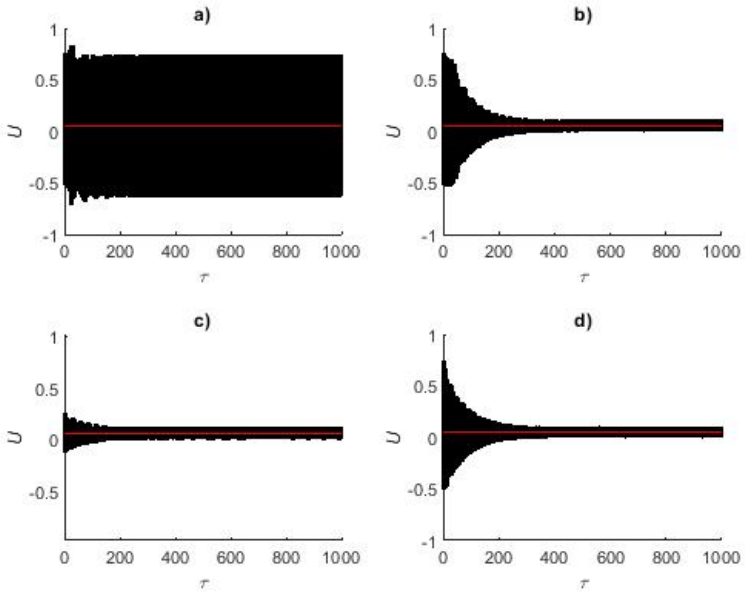

Fig. 4.18 van der Waals, 6T ROM Time Responses, $\delta = 4$, $b = 0.025$, $\alpha = 0$, $\mu = 0.2$: a) $U_0 = 0.75$, $\sigma = -0.12$, b) $U_0 = 0.75$, $\sigma = -0.125$, c) $U_0 = 0.25$, $\sigma = -0.12$, d) $U_0 = 0.75$, $\sigma = -0.15$

and C. However, MMS predicts the amplitude-frequency response quite well in the case of higher damping and/or low voltage. Secondary resonance superharmonic of second-order has been reported in the literature (Kim and Lee, 2015; Liu et al, 2014), for *AC* electrostatic actuation and for different structures than plates. Najar et al (2010); Kim and Lee (2015) have shown similar results, although for different structures and a hardening effect rather than softening effect as in this research.

In this paper two models for hard excitations were used for MMS, a one term no epsilon model (1TnE) and a two term no epsilon model (2TnE) for the electrostatic actuation. 2TnE was the most accurate of the two and it was used to investigate the effect of the degrees of the MMS Taylor polynomials approximating electrostatic, Casimir and van der Waals forces. This investigation showed that beyond the Taylor polynomial of 25th degree, there is no significant difference in the predictions. The ROM shows various benefits when compared to the MMS models. 6T ROM AUTO was able to predict the endpoints B and C, and the stable branches are in agreement wit the predictions of time responses. Furthermore, the convergence of the ROM showed that 6T ROM was deemed sufficient for this research. These methods were used to investigate the effects influences of different parameters, such as voltage, and damping on the amplitude-frequency response. Increasing the voltage led to a stronger nonlinear behavior, such as the appearance of the unstable branch 2, when

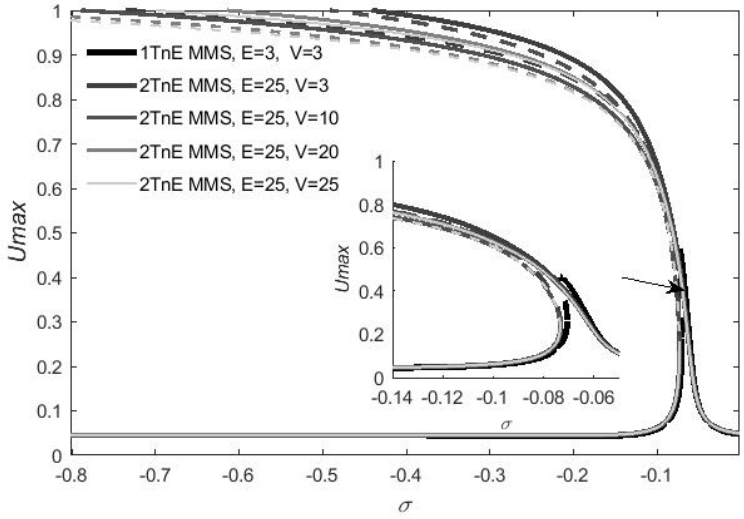

Fig. 4.19 Effect of V, the degree of the Taylor polynomial approximating the van der Waals force in MMS on the amplitude-frequency response using 1TnE MMS $E = 3$ and 2TnE MMS $E = 25$, $\delta = 4$, $b = 0.025$, $\alpha = 0$, $\mu = 0.2$, E is the degree of the electrostatic Taylor polynomial, V is the degree of the van der Waals Taylor polynomial.

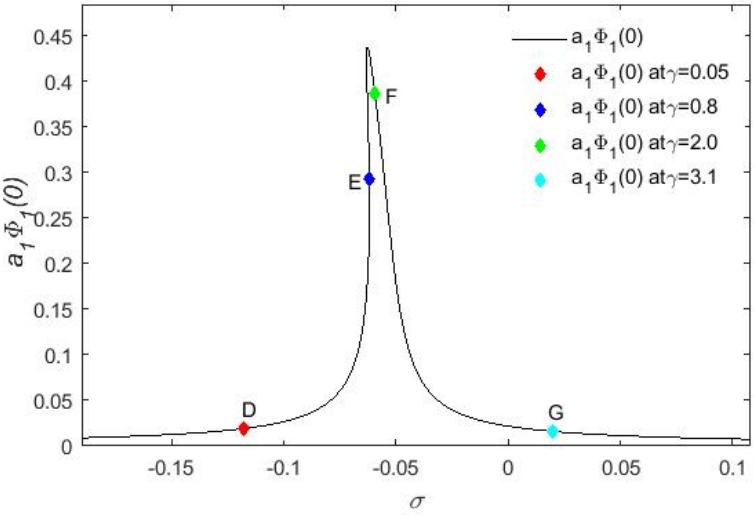

Fig. 4.20 Stability Testing, $\delta = 4$, $b = 0.025$, $\alpha = 0$, $\mu = 0.2$

the branches were split. Increasing damping led to a more linear behavior. The increase of the Casimir and the van der Waals parameters, led to an increase of the softening effect, and therefore a decrease of higher amplitudes. The lower amplitudes did not differ from the electrostatic models.

References

Ahmad B, Pratap R (2010) Elasto-electrostatic analysis of circular microplates used in capacitive micromachined ultrasonic transducers. IEEE Sensors Journal 10(11):1767–1773

Anjomshoa A, Tahani M (2016) Vibration analysis of orthotropic circular and elliptical nano-plates embedded in elastic medium based on nonlocal Mindlin plate theory and using Galerkin method. Journal of Mechanical Science and Technology 30(6):2463–2474

Ashoori A, Vanini SS, Salari E (2017) Size-dependent axisymmetric vibration of functionally graded circular plates in bifurcation/limit point instability. Applied Physics A 123(4):1–14

Baecker D, Kuna M, Haeusler C (2015) Eigenfunctions of crack problems in the Mindlin plate theory. ZAMM-Journal of Applied Mathematics and Mechanics/Zeitschrift für Angewandte Mathematik und Mechanik 95(8):765–777

Batra R, Porfiri M, Spinello D (2008) Reduced-order models for microelectromechanical rectangular and circular plates incorporating the Casimir force. International Journal of Solids and Structures 45(11-12):3558–3583

Caruntu DI, Juarez E (2019) Voltage effect on amplitude–frequency response of parametric resonance of electrostatically actuated double-walled carbon nanotube resonators. Nonlinear Dynamics 98(4):3095–3112

Caruntu DI, Luo L (2014) Frequency response of primary resonance of electrostatically actuated CNT cantilevers. Nonlinear Dynamics 78(3):1827–1837

Caruntu DI, Oyervides R (2016) Voltage response of primary resonance of electrostatically actuated MEMS clamped circular plate resonators. Journal of Computational and Nonlinear Dynamics 11(4):041,021

Caruntu DI, Oyervides R (2017) Frequency response reduced order model of primary resonance of electrostatically actuated MEMS circular plate resonators. Communications in Nonlinear Science and Numerical Simulation 43:261–270

Caruntu DI, Reyes CA (2020) Casimir Effect on Amplitude-Frequency Response of Parametric Resonance of Electrostatically Actuated NEMS Cantilever Resonators. In: Developments and Novel Approaches in Biomechanics and Metamaterials, Springer, pp 267–289

Caruntu DI, Martinez I, Knecht MW (2013) ROM analysis of frequency response of AC near half natural frequency electrostatically actuated MEMS cantilevers. Journal of Computational and Nonlinear Dynamics 8(3):031,011

Caruntu DI, Martinez I, Knecht MW (2016) Parametric resonance voltage response of electrostatically actuated Micro-Electro-Mechanical Systems cantilever resonators. Journal of Sound and Vibration 362:203–213

Caruntu DI, Botello MA, Reyes CA, Beatriz JS (2019) Voltage–amplitude response of superharmonic resonance of second order of rlectrostatically actuated MEMS cantilever resonators. Journal of Computational and Nonlinear Dynamics 14(3):031,005

Caruntu DI, Botello MA, Reyes CA, Beatriz JS (2021) Frequency-amplitude response of superharmonic resonance of second order of electrostatically actuated MEMS resonators. International Journal of Non-Linear Mechanics 133:10,371

Dorfmeister M, Scneider M, Schmid U (2018) Static and dynamic performance of bistable MEMS membranes. Sensors and Actuators A: Physical 282(15):259–268

Ishfaque A, Kim B (2017) Analytical solution for squeeze film damping of MEMS perforated circular plates using Green's function. Nonlinear Dynamics 87(3):1603–1616

Kacem N, Baguet S, Hentz S, Dufour R (2012) Pull-in retarding in nonlinear nanoelectromechanical resonators under superharmonic excitation. Journal of Computational and Nonlinear Dynamics 7(2):021,011

Kahrobaiyan MH, Asghari M, Hoore M, Ahmadian MT (2011) Nonlinear size-dependent forced vibrational behavior of microbeams based on a non-classical continuum theory. Journal of Vibration and Control 18(5):696–711

Khadem S, Rasekh M, Toghraee A (2012) Design and simulation of a carbon nanotube-based adjustable nano-electromechanical shock switch. Applied Mathematical Modelling 36(6):2329–2339

Kim I, Lee S (2015) Nonlinear resonances of a single-wall carbon nanotube cantilever. Physica E: Low-dimensional Systems and Nanostructures 67:159–167

Lee S, Cho C, Kim J, Park S, Yi S, Kim J, Cho DiD (1998) The effects of post-deposition processes on polysilicon Young's modulus. Journal of Micromechanics and Microengineering 8(4):330–337

Liao LD, Chao PC, Huang CW, Chiu CW (2009) DC dynamic and static pull-in predictions and analysis for electrostatically actuated clamped circular micro-plates based on a continuous model. Journal of Micromechanics and Microengineering 20(2):025,013

Lin MX, Lee SY, et al (2018) Dynamic characteristic analysis of an electrostatically-actuated circular nanoplate subject to surface effects. Applied Mathematical Modelling 63:18–31

Liu C, Yue S, Xu Y (2014) Nonlinear resonances of electrostatically actuated nano-beam. Journal of Vibroengineering 16(5):2484–2493

Maurini C, Pouget J, dell'Isola F (2006) Extension of the Euler-Bernoulli model of piezoelectric laminates to include 3D effects via a mixed approach. Computers & Structures 84(22-23):1438–1458

Najar F, Nayfeh A, Abdel-Rahman E, Choura S, El-Borgi S (2010) Nonlinear analysis of MEMS electrostatic microactuators: primary and secondary resonances of the first mode. Journal of Vibration and Control 16(9):1321–1349

Nayfeh AH, Younis MI (2005) Dynamics of MEMS resonators under superharmonic and subharmonic excitations. Journal of Micromechanics and Microengineering 15(10):1840–1847

Nisar A, Afzulpurkar N, Mahaisavariya B, Tuantranont A (2008) MEMS-based micropumps in drug delivery and biomedical applications. Sensors and Actuators B: Chemical 130(2):917–942

Ouakad HM (2017) Comprehensive numerical modeling of the nonlinear structural behavior of MEMS/NEMS electrostatic actuators under the effect of the van der Waals forces. Microsystem Technologies 23(12):5903–5910

Rahim FC (2010a) A numerical approach to investigate of pull-In phenomenon of circular micro plate subjected to nonlinear electrostatic pressure. Sensors & Transducers 117(6):41–49

Rahim FC (2010b) Investigation Effect of Residual Stress on Pull-In Voltage of Circular Micro Plate Subjected to Nonlinear Electrostatic Force. Sensors & Transducers 123(12):25

Rao SS (2007) Vibration of Continuous Systems: John Wiley & Sons. New Jersey

Sajadi B, Alijani F, Goosen H, van Keulen F (2018) Effect of pressure on nonlinear dynamics and instability of electrically actuated circular micro-plates. Nonlinear Dynamics 91(4):2157–2170

Shabani R, Sharafkhani N, Tariverdilo S, Rezazadeh G (2013) Dynamic analysis of an electrostatically actuated circular micro-plate interacting with compressible fluid. Acta Mechanica 224(9):2025–2035

Sharafkhani N, Rezazadeh G, Shabani R (2012) Study of mechanical behavior of circular FGM micro-plates under nonlinear electrostatic and mechanical shock loadings. Acta Mechanica 223(3):579–591

Sharpe WN, Yuan B, Vaidyanathan R, Edwards RL (1997) Measurements of Young's modulus, Poisson's ratio, and tensile strength of polysilicon. In: Proceedings IEEE the Tenth Annual International Workshop on Micro Electro Mechanical Systems. An Investigation of Micro Structures, Sensors, Actuators, Machines and Robots, IEEE, pp 424–429

Varona J, Tecpoyotl-Torres M, Hamoui A (2007) Modeling of MEMS thermal actuation with external heat source. In: Electronics, Robotics and Automotive Mechanics Conference (CERMA 2007), IEEE, pp 591–596

Wang YN, Fu LM (2018) Micropumps and biomedical applications–A review. Microelectronic Engineering 195:121–138

Zhang Jh, Ma Sl, Qin Lf (2015) Analysis of frequency characteristics of MEMS piezoelectric cantilever beam based energy harvester. In: 2015 Symposium on Piezoelectricity, Acoustic Waves, and Device Applications (SPAWDA), IEEE, pp 193–197

Zietlow DW, Griffin DC, Moore TR (2012) The limitations on applying classical thin plate theory to thin annular plates clamped on the inner boundary. AIP Advances 2(4):042,103